

# 1 Role of Indian Ocean basin mode in driving the interdecadal 2 variations of summer precipitation over the East Asian monsoon 3 boundary zone

4  
5 Jing Wang<sup>1,\*</sup>, Yanju Liu<sup>2</sup>, Fei Cheng<sup>3,\*</sup>, Chengyu Song<sup>4</sup>, Qiaoping Li<sup>5</sup>, Yihui Ding<sup>2</sup>, Xiangde Xu<sup>6</sup>

6 <sup>1</sup>Tianjin Key Laboratory for Oceanic Meteorology, and Tianjin Institute of Meteorological Science, Tianjin, China

7 <sup>2</sup>National Climate Center, China Meteorological Administration, Beijing, China

8 <sup>3</sup>Ningbo Meteorological Observatory, Ningbo, China

9 <sup>4</sup>Heilongjiang Climate Centre, Harbin, China

10 <sup>5</sup>CMA Earth System Modelling and Prediction Centre, Beijing, China

11 <sup>6</sup>State Key Laboratory of Severe Weather, Chinese Academy of Meteorological Sciences, Beijing, China

12  
13 Correspondence: Yanju Liu (liuyan@cmac.gov.cn)

14 \* Jing Wang and Fei Cheng contributed equally to this work.

15  
16 **Abstract.** Based on long-term observational and reanalysis datasets from 1901 through 2014, this study investigates the  
17 characteristics and physical causes of the interdecadal variations in the summer precipitation over the East Asian monsoon  
18 boundary zone (EAMBZ). Observational evidence reveals that the EAMBZ precipitation featured prominent interdecadal  
19 fluctuations, e.g., with dry summers during the periods preceding 1927, 1939–1945, 1968–1982, and 1998–2010, and wet  
20 summers during the periods of 1928–1938, 1946–1967, and 2011 onwards. Further analyses identify that the Indian Ocean  
21 basin mode (IOBM) is an important oceanic modulator responsible for the interdecadal variations of the EAMBZ  
22 precipitation. When the cold phase of the IOBM occurs, an anomalous cyclonic circulation is excited around the northeast  
23 corner of the tropical Indian Ocean, which further induces a “north-low–south-high” meridional seesaw pattern over the  
24 Northeast China–subtropical western Pacific (SWP) sector. Such seesaw pattern is conducive to the enhanced EAMBZ  
25 precipitation through linking favorable environments for the transportation of water vapor from the SWP and the  
26 convergence over EAMBZ at interdecadal timescales. For this reason, a physical-empirical model for the EAMBZ  
27 precipitation is developed in terms of the IOBM cooling, which can well capture its interdecadal fluctuations and reflect  
28 their steady relationship. The key physical pathway connecting the IOBM cooling with the interdecadal variations of the  
29 summer EAMBZ precipitation is supported by the numerical results based on the large ensemble experiment and the  
30 Indian Ocean pacemaker experiment. Our findings may provide new insights into the understanding of the causes of the  
31 interdecadal variations in the summer EAMBZ precipitation, which may favor the long-term policy decision making for  
32 the local hydrometeorological planning.

## 33 34 1 Introduction

35  
36 The monsoonal airflows and mid-latitude westerlies are crucial components of the Asian climate system (Li and Zeng,  
37 2002; Ding and Chan, 2005; Wang et al., 2008; Wu et al., 2012; Huang et al., 2015; Wang et al., 2017; Chen et al., 2018;  
38 J. Huang et al., 2019). These two subsystems can synergistically induce regional precipitation fluctuations over  
39 subtropical and mid-latitude Asia during the Northern Hemisphere late spring (May) and summer (June–July–August;  
40 JJA) (Qian et al., 2009; Chen et al., 2021; Song et al., 2022; J. Wang et al., 2022). For example, Song et al. (2022) found  
41 that May precipitation over the southeastern extension of the Tibetan Plateau (TP) features notable year-to-year variations,  
42 which are physically linked to a unique interplay between the upstream mid-latitude westerlies and the Bay of Bengal  
43 summer monsoon.

44

45 During the early stage of the northern summer, however, the mid-latitude westerlies shift poleward to the north of the TP  
46 abruptly (Yeh et al., 1959; Schiemann et al., 2009). In this context, westerlies of mid-latitude synoptic disturbance and  
47 southerlies of East Asian summer monsoon (EASM) collide with each other frequently over the East Asian monsoon  
48 boundary zone (EAMBZ) (Qian et al., 2009; Wang et al., 2017; Chen et al., 2018; J. Huang et al., 2019; Zeng and Zhang,  
49 2019; Chen et al., 2021; Q. Wang et al., 2021, 2022, 2023). EAMBZ is a transitional climate zone between the EASM-  
50 controlled moist region and the westerly-dominated arid region over central Asia (Chen et al., 2010; Chen et al., 2018,  
51 2021), stretching from the eastern flank of the TP to Mongolia and Northeast China [see Fig. 1 in Chen et al. (2021)]; also  
52 see the red box in Fig. 1]. Notably, EAMBZ is a distinguished region with agrarian economy and animal husbandry, which  
53 is largely susceptible to water resource variations (Ou and Qian, 2006; Lu and Jia, 2013). Nevertheless, many studies  
54 reported that in the past century, the semi-arid EAMBZ underwent the most profound warming over East Asia, suffering  
55 from serious aridification and a high risk of desertification (J. Huang et al., 2017, 2019, 2020). In this regard, EAMBZ is  
56 deemed one of the “hotspots” highly sensitive to precipitation fluctuations (Qian et al., 2009; Lu and Jia, 2013; J. Huang  
57 et al., 2019). Given that the EAMBZ is of an ecologically fragile environment with water shortage, a deep understanding  
58 of the reasons for historical changes in summer EAMBZ precipitation could be a prerequisite for in situ ecological  
59 improvement and socioeconomic development.

60

61 Existing studies have well documented physical mechanisms responsible for the interannual variability of summer  
62 EAMBZ precipitation, highlighting the external moisture supply pathways, the modulators for the wet-dry condition  
63 variations [e.g., the mid-latitude westerlies within the Asian westerly jet, the western North Pacific subtropical high, and  
64 the EASM], and the remote modulation roles of large-scale teleconnected modes [e.g., Silk Road pattern/circumglobal  
65 teleconnection propagating along the westerly jet and the Eurasian teleconnection] and sea surface temperature (SST)  
66 anomaly patterns (Huang et al., 2015; Wang et al., 2017; Chen et al., 2018, 2021; Zhao et al., 2019a, 2019b, 2020; Q.  
67 Wang et al., 2021, 2022, 2023). For instance, Q. Wang et al. (2022) suggested that the positive phase of the Eurasian  
68 teleconnection is connected with a low pressure anomaly in the lower troposphere in EAMBZ and the Mongolia region,  
69 thus favoring enhanced summertime precipitation over EAMBZ; and meanwhile, the circumglobal teleconnection is  
70 positively coupled with the EAMBZ precipitation, with ascending motion anomalies over EAMBZ during its positive  
71 phase. Chen et al. (2021) established that the circulations (i.e., the mid-latitude westerlies and EASM) and the forcing of  
72 SST anomalies (SSTAs) can collectively regulate the summer EAMBZ precipitation variability. The variability of  
73 westerlies is largely modulated by the Silk Road pattern and the meridional displacement of the westerly jet; while the  
74 EASM variability is mainly modulated by the prior wintertime El Niño-Southern Oscillation. The synchronized effects  
75 of EASM and westerlies largely contribute to the rainfall variability in EAMBZ. Note that Chen et al. (2021) also pointed  
76 out that the Indian Ocean basin mode (IOBM) is simultaneously correlated with the EASM in boreal summer on the  
77 interannual timescale, which may be considered as a salient oceanic modulator for the summer EAMBZ precipitation  
78 variability. Nevertheless, they paid little attention to the physical mechanisms of how IOBM regulates the year-to-year  
79 EAMBZ precipitation. Moreover, Zhao et al. (2019a) found that the tropical northern Atlantic SSTAs have significant  
80 impacts on the August rainfall over the monsoon transitional zone in China through inducing a wavetrain over Eurasia  
81 and the western North Pacific anomalous anticyclone.

82

83 Compared with the extensively explored interannual variability of the JJA EAMBZ precipitation, less efforts have been  
84 devoted to its interdecadal variability. To understand and predict the summer EAMBZ precipitation, exploring its  
85 interdecadal variations and the underlying physical causes are also critical, which are the main focus of the present study.  
86 Previous studies suggested that the warm-season precipitation over many Asian areas features interdecadal fluctuations.

87 For example, [J. Wang et al. \(2022\)](#) reported that the late spring (May) southeastern TP underwent wet conditions for  
88 1928–1961 and 1989–2003, and experienced dry conditions preceding 1927, 1962–1988, and 2004 onwards. [Si and Ding](#)  
89 [\(2016\)](#) documented that East Asia experienced dry summers from the early 1920s to the 1940s, as well as wet summers  
90 from the late 1900s to the early 1920s, in the 1950s, and from the 1980s to the 1990s. [Piao et al. \(2021\)](#) found that the  
91 decadal-filtered summer precipitation over Northeast Asia underwent a sudden decrease around the late 1990s. The oceanic  
92 interdecadal signals for these interdecadal changes are also extensively investigated, highlighting the crucial modulation  
93 roles of basin-scale SST modes of Atlantic multidecadal oscillation, Pacific decadal oscillation/interdecadal Pacific  
94 oscillation (IPO), and IOBM ([Si et al., 2021](#)). Among these interdecadal oceanic forcings, it is essential to emphasize the  
95 IOBM, a dominant mode of SST variability in the tropical Indian Ocean (TIO) sector, which usually follows up a  
96 wintertime El Niño-Southern Oscillation event and persists into the summer through the capacitor effect ([Klein et al.,](#)  
97 [1999](#); [Yang et al., 2007](#); [Xie et al., 2009](#)). It is worth noting that the IOBM also features a basin-scale warming/cooling at  
98 interdecadal timescales ([Han et al., 2014](#)), exerting active impacts on the mid-latitude Asian climate (e.g., [Wu et al., 2016](#);  
99 [Li and Ma, 2018](#); [Zhang et al., 2018](#); [S. Wang et al., 2022](#)). As for the interdecadal variations of the summer EAMBZ  
100 precipitation, we hope to answer the following two questions: 1) Did the JJA EAMBZ precipitation feature interdecadal  
101 variations? If so, 2) is there any intimate connection between IOBM and the EAMBZ precipitation at interdecadal  
102 timescales? As such, this study shall extend previous studies by exploring what extent and how the JJA IOBM modulate  
103 the concurrent EAMBZ precipitation variability at interdecadal timescales, with the aim of providing a novel  
104 understanding for the rainfall variability over the mid-latitude semi-arid zone in Asia. Note that we employ datasets with  
105 a centennial scale in this study [e.g., the precipitation data produced by the Climatic Research Unit (CRU) and the  
106 atmospheric circulation data from the Twentieth Century Reanalysis datasets]. In comparison with the short-term datasets  
107 since the latter half of the 20th century, these long-term datasets can separate the interdecadal variability of EAMBZ  
108 precipitation from the externally forced global climate change caused by anthropogenic (e.g., greenhouse gas) and natural  
109 forcings (e.g., volcanic eruption) more effectively ([Wu et al., 2016](#)), which were widely used to investigate the physical  
110 causes of how internal fluctuations of the climate system modulate the interdecadal variations of precipitation over Asia  
111 (e.g., [Wu et al., 2016](#); [Zhang et al., 2018](#); [Sun et al., 2019a](#); [Jiang et al., 2021](#); [J. Wang et al., 2022](#)).

112  
113 The remainder of this paper is arranged as follows. Section 2 describes the datasets and methods used in this study. Section  
114 3 elucidates the characteristics of the interdecadal variations of summertime EAMBZ precipitation and the associated  
115 background circulations, illustrates the mechanisms of how IOBM modulates the EAMBZ precipitation, establishes a  
116 linear regression model using the IOBM to predict the interdecadal precipitation anomalies over EAMBZ, and verifies  
117 the IOBM-related physical processes using numerical model simulations. A summary of the major findings and further  
118 discussions are provided in Section 4.

119

## 120 **2 Datasets and methods**

121

### 122 **2.1 Observational Data**

123

124 Several monthly mean observational datasets are utilized in the present study, including (1) the global land high-resolution  
125 gridded CRU time series precipitation dataset version 3.26 (CRU TS3.26; spatial resolution:  $0.5^\circ \times 0.5^\circ$ ; [Harris et al., 2014](#))  
126 for 1901–2017, (2) the Extended Reconstructed SST version 5 (ERSSTv5; spatial resolution:  $2^\circ \times 2^\circ$ ; [B. Huang et al., 2017](#))  
127 for 1854–present derived from the National Oceanic and Atmospheric Administration (NOAA), and (3) atmospheric  
128 variables derived from NOAA–Cooperative Institute for Research in Environmental Sciences (CIRES) Twentieth Century  
129 Reanalysis version 2c (20CRv2c; spatial resolution:  $2^\circ \times 2^\circ$ ; [Compo et al., 2011](#)), except for the precipitation data, with

130 192 points in longitude and 94 points in latitude, for 1851–2014. Note that all observational datasets cover the common  
131 time period of 1901–2014, which is the focused period in the present research.

132

## 133 2.2 Rossby wave source

134

135 Following [Sardeshmukh and Hoskins \(1988\)](#), the Rossby wave source (RWS) is calculated as:

$$136 \text{RWS} = -\nabla \cdot [\mathbf{V}_z (\zeta + f)], \quad (1)$$

137 where  $\mathbf{V}_z$  is the divergent wind,  $\zeta$  is the relative vorticity, and  $f$  is the planetary vorticity.

138

## 139 2.3 Moisture flux and associated divergence

140

141 The vertically integrated horizontal water vapor transport ( $\langle \text{WVT} \rangle$ ) and WVT-associated divergence ( $\langle \text{WVT\_div} \rangle$ ) are  
142 calculated using the following equations ([Sun et al., 2019b](#); [J. Wang et al., 2022](#)):

$$143 \langle \text{WVT} \rangle = -\frac{1}{g} \int_{P_s}^{300} q \bar{\mathbf{V}} dp, \quad (2)$$

$$144 \langle \text{WVT\_div} \rangle = -\frac{1}{g} \int_{P_s}^{300} \nabla_p \cdot (q \bar{\mathbf{V}}) dp, \quad (3)$$

145 where  $\nabla_p \cdot ()$  denotes the horizontal divergence in the pressure coordinates;  $g$  is the gravitational acceleration;  $P_s$  is the

146 surface pressure;  $q$  is the specific humidity; and  $\bar{\mathbf{V}} = (u, v)$  is the horizontal wind vector ( $u$  and  $v$  represent the zonal and

147 meridional winds, respectively).

148

## 149 2.4 Statistical methods

150

151 This study focuses on interdecadal fluctuations in variables. The data are 11-year low-pass filtered by adopting a Lanczos  
152 filter ([Duchon, 1979](#)) to extract the corresponding interdecadal signal. Several statistical methods are used, including  
153 empirical orthogonal function (EOF) analysis, composite analysis, correlation analysis, and linear regression analysis. A  
154 two-tailed Student's  $t$  test is used to evaluate the statistical significance. Considering the 11-year low-pass filtered method  
155 can significantly reduce the degrees of freedom of the data, the following approximation is therefore deployed to calculate  
156 the effective degrees of freedom ( $N^{\text{eff}}$ ):

$$157 \frac{1}{N^{\text{eff}}} \approx \frac{1}{N} + \frac{2}{N} \sum_{j=1}^N \frac{N-j}{N} \rho_{XX}(j) \rho_{YY}(j), \quad (4)$$

158 where  $N$  is the sample size, and  $\rho_{XX}(j)$  and  $\rho_{YY}(j)$  are the autocorrelations of two sampled time series  $X$  and  $Y$ ,  
159 respectively, at time lag  $j$  ([Li et al., 2013](#)).

160

161 In this study, we focus on the boreal summer season (JJA). All variables in observations and model simulations are  
162 linearly detrended before further calculations and analyses to exclude potential impacts of long-term trends.

163

## 164 2.5 Definitions

165

## 166 2.5.1 The research domain of EAMBZ

167

168 From the long-term (1901–2014) perspective of the climatological mean state of converged  $\langle WVT \rangle$  and pronounced  
169 precipitation over the mid-latitude Asia, the EAMBZ (box in **Figs. 1a** and **1b**;  $35^{\circ}$ – $55^{\circ}$ N,  $105^{\circ}$ – $130^{\circ}$ E) is defined as the  
170 collision and convergence zone between JJA dry westerly  $\langle WVT \rangle$  and moist southwesterly  $\langle WVT \rangle$  (**Fig. 1a**). As such,  
171 there exist wetter conditions over the EASM-dominated part and drier conditions over the westerly-controlled part (**Fig.**  
172 **1b**), suggesting the semi-arid transitional feature of EAMBZ (Xing and Wang, 2017). Our defined research domain of  
173 EAMBZ largely matches the monsoon boundary zone defined by Chen et al. (2021), covering Inner Mongolia, Gansu,  
174 Ningxia, Shaanxi, Shanxi, Hebei, Beijing, Tianjin, Shandong, Jilin, Liaoning, and Heilongjiang in China, as well as  
175 eastern Mongolia and Korean peninsula. Note that the areal mean precipitation over EAMBZ in boreal summer is the  
176 highest of the year accompanying the largest standard deviation (i.e., largest rainfall variability) (**Fig. S1**), which is the  
177 focused season in the present study.

178

## 179 2.5.2 Climate indices

180

181 The IOBM index ( $I_{IOBM}$ ) is defined as areal mean SSTAs over the TIO domain of  $20^{\circ}$ S– $20^{\circ}$ N,  $40^{\circ}$ – $100^{\circ}$ E (Xie et al.,  
182 2009). The IPO index is calculated using a method identical to that defined in Henley et al. (2015), that is, the difference  
183 between SSTAs averaged over the central equatorial Pacific ( $10^{\circ}$ S– $10^{\circ}$ N,  $170^{\circ}$ E– $90^{\circ}$ W) and the average of SSTAs in the  
184 northwest ( $25^{\circ}$ – $45^{\circ}$ N,  $140^{\circ}$ E– $145^{\circ}$ W) and the southwest Pacific ( $50^{\circ}$ S– $15^{\circ}$ S,  $150^{\circ}$ E– $160^{\circ}$ W). In observations,  
185 considering the coupled nature of IOBM and IPO at interdecadal timescales in boreal summer [cf. Fig. 2a in Wu et al.  
186 (2016)], we hence remove the potential influence of the contemporaneous IPO on precipitation via eliminating the signal  
187 of IPO index from the data of climate variables based on the partial regression technique, which is widely used in previous  
188 studies (e.g., Dou and Wu, 2018; J. Wang et al., 2022).

189

## 190 2.6 Model simulations

191

192 To validate our proposed mechanisms of how the TIO SSTAs (i.e., IOBM-associated SSTAs) remotely modulate the  
193 summer EAMBZ precipitation on interdecadal timescales, following the method of Zhang et al. (2019) and Yang et al.  
194 (2020), we adopt monthly mean outputs from two experiments of the Community Earth System Model version 1 (CESM1),  
195 which is a fully coupled Earth system model incorporating components of atmosphere, ocean, land, and sea ice (Hurrell  
196 et al., 2013).

197

198 The first experiment is the CESM1 Large Ensemble Numerical Simulation (referred to as CESM1\_LENS; Kay et al.,  
199 2015). Among total 40 ensemble members in CESM1\_LENS (Yang et al., 2020), we use the first 35 individual members  
200 according to many previous studies (e.g., Touma et al., 2021; J. Wang et al., 2023), which were completed at the climate  
201 modeling center of National Center for Atmospheric Research (NCAR). Note that all ensemble members in  
202 CESM1\_LENS were imposed with the same radiative forcing scenario (Taylor et al., 2012), with historical forcing for  
203 1920–2005 and high-emission forcing scenario (i.e., Representative Concentration Pathway 8.5) for 2006–2080 (Moss et  
204 al., 2010; Touma et al., 2021). The ensemble members were further generated with slightly differentiated perturbations  
205 of atmospheric states (Kay et al., 2015; Touma et al., 2021). The second experiment is the CESM1 Indian Ocean  
206 Pacemaker Ensemble Simulation (referred to as CESM1\_IOPES), with 10 ensemble members (Zhang et al., 2019; Yang  
207 et al., 2020). We adopt CESM1\_IOPES to highlight the impact of SSTAs over the broader TIO domain ( $15^{\circ}$ S– $15^{\circ}$ N,  
208 African coast to  $174^{\circ}$ E). For the convenience of subsequent calculations and analyses, the African coast is designated as

209 40°E in this study, and a small change in the longitudes regarding the African coast may not affect the main results.

210

211 As indicated by Yang et al. (2020), the CESM1\_LENS 35-member ensemble mean results can better provide an estimate  
212 of the influence of the external radiative forcing signals (e.g., greenhouse gas) on the climate system. Furthermore, the  
213 10-member ensemble mean results in CESM1\_IOPES contain the responses to both external forcings and the observed  
214 SST variations over the TIO domain (Yang et al., 2020). Therefore, by subtracting the CESM1\_LENS ensemble mean  
215 from the CESM1\_IOPES ensemble mean, we can obtain responses of the climate system to the internal variability  
216 stemming from the time-varying TIO SSTAs, distinguishing the impact of external radiative force changes from the  
217 intrinsic variability driven by TIO SSTAs. More details about CESM1\_LENS and CESM1\_IOPES can be found in Kay  
218 et al. (2015) and Yang et al. (2020), respectively. The variables employed here comprise precipitation and wind in  
219 atmosphere component of Community Atmospheric Model version 5, with a spatial resolution of 1.25° in longitude and  
220 0.9° in latitude; and SST in the ocean component of Parallel Ocean Program version 2, with 320 grids in longitude and  
221 384 grids in latitude. Before further analyses, model outputs are interpolated at a resolution of 2°×2° using a bilinear  
222 interpolation method (Mastyło, 2013), identical to that of 20CRv2c. In the current study, we focus on the historical  
223 simulation period of 1920–2005.

224

225 Here, it is important to stress the following two points. First, although the TIO domain in CESM1\_IOPES is broader than  
226 that for defining  $I_{IOBM}$ , there exist highly consistent temporal variations in SSTAs between them in observations (Fig. S2)  
227 and simulations (Fig. S3) at interdecadal timescales, with temporal correlation coefficients (TCCs) of 0.93 and 0.87 ( $P <$   
228 0.01), respectively. Second, when selecting the SSTAs over the broader TIO domain (purple box in Fig. S4) as a metric,  
229 it can be found that the observed (Fig. S4a) and modelled (Fig. S4b) large and intense loadings of the positive SSTAs are  
230 still concentrated around the narrower TIO domain (black box in Fig. S4). As such, it is plausible to adopt the above-  
231 mentioned Indian Ocean pacemaker experiment with broader TIO SSTAs to validate our proposed mechanisms tied to  
232 the interdecadal IOBM variations.

233

## 234 3 Results

235

### 236 3.1 Observed interdecadal variations of the summer precipitation over EAMBZ and related 237 background circulations

238

239 Figure 1c plots the spatial distribution of the interdecadal standard deviation of precipitation. This distribution is quite  
240 similar to that of the climatology (Fig. 1b), suggesting relatively strong (weak) interdecadal precipitation fluctuations  
241 over the EASM-dominated (westerly-controlled) part of the EAMBZ. Moreover, we show the first EOF mode of JJA-  
242 mean EAMBZ precipitation (Fig. 1d), which accounts for 28% of the total variance and distinguishes from the remaining  
243 eigenvectors according to the criterion defined by North et al. (1982). The leading EOF mode bears close resemblance to  
244 the standard deviation of the EAMBZ precipitation on interdecadal timescales (Figs. 1c and 1d), with larger loadings  
245 occupying the Bohai Sea and Korean peninsula and their adjoining regions. The interdecadal TCC between the principal  
246 component of the EOF1 and area-averaged precipitation over the research domain of EAMBZ (35°–55°N, 105°–130°E)  
247 [EAMBZ precipitation index ( $I_{EAMBZP}$  for short); Fig. 1e] is 0.93 ( $P < 0.001$ ). The aforementioned results indicate that  
248 that our defined  $I_{EAMBZP}$  can serve as a good indicator of the predominant fluctuations in the precipitation anomalies over  
249 EAMBZ at interdecadal timescales. As such, from the time series of 11-year low-passed filtered  $I_{EAMBZP}$  (Fig. 1e), we can  
250 observe that the summer EAMBZ precipitation delineates notable interdecadal fluctuations. For example, EAMBZ  
251 experienced dry summers during the periods preceding 1927, 1939–1945, 1968–1982, and 1998–2010, but underwent

252 wet summers during the periods of 1928–1938, 1946–1967, and 2011 onwards. Note that [Si et al. \(2021\)](#) explored the  
253 interdecadal variations of summer precipitation over northeast Asian, a domain that largely matches our focused EAMBZ  
254 domain. The observed major interdecadal fluctuation periods of EAMBZ precipitation are basically consistent with those  
255 suggested by [Si et al. \(2021\)](#), with dry summers around 1940.

256

257 Before examining the modulation of IOBM on the interdecadal EAMBZ precipitation fluctuations, it is essential to  
258 scrutinize the JJA-mean  $I_{\text{EAMBZP}}$ -associated circulation anomalies. The highest mid-latitude positive correlation region  
259 can be discerned north of the TP ( $38^{\circ}$ – $46^{\circ}$ N,  $80^{\circ}$ – $112.5^{\circ}$ E; blue box in **Fig. 2a**), suggesting that the interdecadal  
260 enhancement of the summer EAMBZ precipitation is intimately correlated with the acceleration of the upstream mid-  
261 latitude westerlies at 400 hPa. In light of the method of [Chen et al. \(2021\)](#) and [J. Wang et al. \(2022\)](#), we correlate the  
262  $I_{\text{EAMBZP}}$  with the zonal winds averaged over the longitudinal range of EAMBZ at multiple levels (**Fig. 2b**) to further check  
263 whether the most significant correlation occurs at 400 hPa. Evidently, on interdecadal timescales, the largest positive  
264 correlation between precipitation and mid-latitude westerlies within  $38^{\circ}$ – $46^{\circ}$ N does occur at the mid-tropospheric level  
265 of 400 hPa, with a TCC of 0.46 ( $P < 0.01$ ) between the  $I_{\text{EAMBZP}}$  and areal mean 400-hPa zonal winds over the upstream  
266 westerly-dominated domain (**Fig. 2c**). Note that this correlation pattern exhibits a barotropic structure (**Fig. 2b**).  
267 Additionally, we correlate the  $I_{\text{EAMBZP}}$  with the 850-hPa meridional winds. The  $I_{\text{EAMBZP}}$  is positively correlated with the  
268 key monsoonal southerly domain east of the TP ( $25^{\circ}$ – $33^{\circ}$ N,  $102.5^{\circ}$ – $112.5^{\circ}$ E; green box in **Fig. 2d**), which is located in  
269 the western portion of the EASM domain ([Ying et al., 2023](#)). The interdecadal correlation pattern between meridional  
270 winds and the summer EAMBZ precipitation at multiple levels exhibits a baroclinic structure, with the significant positive  
271 correlations confined below 500 hPa (**Fig. 2e**). Note that the strongest positive correlation is detected at 850 hPa within  
272  $102.5^{\circ}$ – $112.5^{\circ}$ E, with a TCC of 0.63 (**Fig. 2f**;  $P < 0.001$ ) between  $I_{\text{EAMBZP}}$  and areal mean 850-hPa meridional winds over  
273 the key EASM-controlled domain (**Fig. 2d**).

274

275 **Figure 3** gives the JJA-mean  $I_{\text{EAMBZP}}$ -regressed circulation anomalies at interdecadal timescales. The interdecadal  
276 enhancement of the EAMBZ precipitation is significantly linked to a localized quasi-barotropic cyclonic (low-pressure)  
277 anomaly. At 400 hPa, significant westerly anomalies prevail in its southern flank, inducing the acceleration of westerlies  
278 upstream of EAMBZ (**Fig. 3a**). At 850 hPa, the enhanced EAMBZ precipitation is connected to a north-south meridional  
279 seesaw pattern, with a significant anticyclonic (high-pressure) anomaly over the subtropical western Pacific (SWP) and a  
280 significant cyclonic anomaly over EAMBZ (**Fig. 3b**), exhibiting a somewhat barotropic structure (**Figs. 3a and 3b**).  
281 Significant southerly anomalies prevail in the western flank of this SWP clockwise gyre anomaly (SWPCGA). Moreover,  
282 from the perspective of  $\langle \text{WVT} \rangle$  (**Fig. 3c**), the magnitudes of southerly  $\langle \text{WVT} \rangle$  anomalies over the key EASM-controlled  
283 domain tied to the SWPCGA are much greater than the westerly  $\langle \text{WVT} \rangle$  anomalies over the westerly-dominated domain.  
284 Note that the southerly  $\langle \text{WVT} \rangle$  anomalies are significantly divergent, pushing copious amounts of warm and moist vapor  
285 over the SWP into EAMBZ. Then, with the aid of the local anticlockwise  $\langle \text{WVT} \rangle$  gyre pattern (**Fig. 3c**), the EASM  
286 southerlies from the low latitudes, which bring warm temperature advection anomalies, may easily collide with the mid-  
287 level cold temperature advection anomalies brought by mid-latitude enhanced westerlies (**Figs. 4a and 4b**), manifesting  
288 the extratropical–tropical interplay around EAMBZ on interdecadal timescales. Such interplay is basically aligned with  
289 that on interannual timescales (cf. [Chen et al., 2021](#)). Under such environments, atmospheric instability over EAMBZ can  
290 be triggered to generate in situ significant ascending motion anomalies responsible for increased precipitation (**Fig. 5a**).  
291 Note that considering the greater magnitudes of anomalies of  $\langle \text{WVT} \rangle$  and warm temperature advection connected to the  
292 southerlies over the key EASM-controlled domain, we presume that the monsoonal southerlies play a predominant  
293 dynamical role in the interdecadal enhancement of precipitation over EAMBZ. To verify this presumption, we further  
294 propose an East Asian monsoon index ( $I_{\text{MI}}$  for short), defined as the areal mean meridional winds at 850 hPa over the key

295 monsoonal southerly domain, and a westerly index ( $I_{WI}$  for short), defined as the areal mean 400-hPa zonal winds over  
296 the upstream westerly-dominated region. The  $I_{MI}$ -regressed results can well and realistically reproduce the magnitudes  
297 and distributions of the anomalous upward motions tied to  $I_{EAMBZP}$  (**Fig. 5b** vs. **5a**). However, the magnitudes of  $I_{WI}$ -  
298 regressed results are highly weakened, along with the major loadings shifting more southward (**Fig. 5c**). Above results  
299 could allow us to conclude that the anomalous southerlies over the key monsoonal southerly domain could be the  
300 predominant driving factor for the interdecadal enhancement of summer EAMBZ precipitation, whereas the upstream  
301 accelerated westerlies play a secondary dynamical amplification role.

302

### 303 **3.2 Interdecadal relationship between IOBM and the summer EAMBZ precipitation**

304

305 Many previous studies have substantiated that the IOBM can remotely modulate summer rainfall fluctuations over the  
306 mid-latitude Asia at interdecadal timescales (e.g., Zhang et al., 2018; S. Wang et al., 2022; Wu et al., 2022). In the present  
307 study, we also identify that the IOBM can exert profound impacts on the interdecadal variations of the EAMBZ  
308 precipitation in boreal summer. In this subsection, we firstly reveal their intimate relationship. **Figure 6a** exhibits the  
309 correlation pattern between the JJA-mean  $I_{EAMBZP}$  and the contemporaneous global gridded SST at interdecadal timescales.  
310 The most pronounced and significant correlations are found in the TIO sector, which largely matches the domain for  
311 delineating the IOBM mode (black frame in **Fig. 6a**). There exists a salient out-of-phase relationship between the  
312 interdecadal EAMBZ precipitation changes and the IOBM mode, with a TCC of  $-0.57$  between  $I_{EAMBZP}$  and  $I_{IOBM}$  (**Fig.**  
313 **6b**;  $P < 0.01$ ). This result suggests that IOBM warming (cooling) is significantly connected with dry (wet) EAMBZ  
314 summers, which serves as a critical oceanic modulator. On interdecadal timescales, the IOBM can remotely spark  
315 conducive dynamical circumstances for increased precipitation over EAMBZ, i.e., the collision between cold and warm  
316 airflows around EAMBZ (**Figs. 4c** and **4d**) and the locally significant convergent ascending motion anomalies resembled  
317 those tied to the positive  $I_{EAMBZP}$  (**Fig. 5d** vs. **5a**). However, the extratropical cold (tropical warm) temperature advection  
318 anomalies west (south) of the EAMBZ, which are tied to the strengthened westerlies (southerlies), are quite insignificant  
319 (significant) (**Figs. 4c** and **4d**). This indicates that the IOBM may exerts a more profound influence on the southerly wind  
320 anomalies over the EASM-controlled domain, which is more important for enhanced EAMBZ precipitation; whereas the  
321 IOBM may insignificantly modulate the westerly anomalies over the westerly-dominated region. The possible underlying  
322 mechanisms of how IOBM links the summertime circulation anomalies responsible for the interdecadal fluctuations in  
323 the EAMBZ precipitation will be illuminated in the next subsection.

324

### 325 **3.3 Possible mechanisms**

326

327 **Figure 7** shows partial regression of the JJA-mean anomalies of SST and large-scale precipitation over TIO and its  
328 neighboring areas onto the  $I_{IOBM}$  at interdecadal timescales with the IPO signal removed. Corresponding to higher  $I_{IOBM}$   
329 years, warm SSTAs cover almost all areas of TIO, with large loadings appearing in the central-southern TIO and relatively  
330 small loadings appearing in the northern TIO (**Fig. 7a**), which are aligned with the previous studies (Wu et al., 2016; Y.  
331 Huang et al., 2019). Moreover, there are striking suppressed precipitation around the northeast corner of the TIO domain  
332 (**Fig. 7b**), suggesting profoundly localized atmospheric responses (viz. the release of regional anomalous atmospheric  
333 cooling) to the warm TIO SSTAs. Note that corresponding to cold TIO SST years, there exist positive precipitation  
334 anomalies around the northeast corner of TIO, suggesting the release of anomalous atmospheric heating (figure not  
335 shown). Since the significant out-of-phase relationship between summertime IOBM and EAMBZ precipitation at  
336 interdecadal timescales, we adopt negative  $I_{IOBM}$ -regressed patterns to express the influence of cold SSTAs over the TIO  
337 region. **Figure 8** displays the anomalous patterns of the RWS, velocity potential, and divergent horizontal winds regressed



338 onto the negative  $I_{IOBM}$ . The velocity potential anomalies with larger negative (positive) loadings in the upper (lower)  
339 troposphere are concentrated surrounding the northeast corner of TIO. Under these circumstances, local upper (lower)  
340 tropospheric divergence (convergence) and negative (positive) RWS anomalies can be observed (**Fig. 8**), suggesting  
341 enhanced ascending motions and convection activities in situ and thereby exciting the localized increased  
342 precipitation/atmospheric heating. The above results indicate that IOBM cooling may transmit its interdecadal influence  
343 via the intermediate atmospheric bridge of enhanced convective activities around the northeast corner of TIO, exerting a  
344 remote modulation on an interdecadal enhancement of the EAMBZ rainfall.

345  
346 Next, we further discuss the physical pathway linking IOBM cooling with the far-reaching downstream circulation  
347 anomalies responsible for the interdecadal enhancement of EAMBZ precipitation, as shown in **Fig. 9**. Because the  
348 cyclonic anomaly at 400 hPa shifts more eastward compared to the  $I_{EAMBZP}$ -regressed counterpart (**Fig. 9a** vs. **3a**), only  
349 fractional westerly anomalies occupy the eastern part of the westerly-dominated region. The TCC between  $I_{IOBM}$  and  $I_{WI}$   
350 is nearly equal to zero ( $r = -0.06$ ), thus linking the insignificant cold temperature advection displayed in **Fig. 4c**.  
351 Nevertheless, in the lower troposphere, a “north-low–south-high” meridional seesaw pattern over the Northeast China–  
352 SWP sector is found to be linked with IOBM cooling (**Fig. 9b**). Note that this negative  $I_{IOBM}$ -regressed seesaw pattern  
353 exhibits a quasi-barotropic structure, with an anticlockwise <WVT> gyre in the north and a SWPCGA in the south (**Fig.**  
354 **9c**), which is highly similar to that shown in **Fig. 3**. Significant anomalies of 850-hPa meridional winds and southerly  
355 <WVT> prevail over the key monsoonal southerly domain, lying on the western flank of SWPCGA (**Figs. 9b** and **c**). The  
356 TCC between  $I_{IOBM}$  and  $I_{MI}$  is  $-0.33$ , significant at 0.05 on interdecadal timescales, thereby linking the significant warm  
357 temperature advection anomalies indicated in **Fig. 4d**.

358  
359 One may ask how IOBM cooling induces the above-mentioned meridional seesaw pattern. Previously, we have revealed  
360 that negative SSTAs over TIO may exert remote interdecadal impacts through an atmospheric bridge, i.e., vigorous  
361 convective activities around the northeast corner of TIO (**Figs. 7** and **8**). In effect, there exists a low-level cyclonic  
362 anomaly in situ (**Fig. 9b**). Such cyclonic anomaly can be interpreted as a typical Gill–Matsuno-type response (Matsuno,  
363 1966; Gill, 1980) to the regional anti-symmetric atmospheric heating caused by IOBM cooling with the coldest center  
364 located south of the equator, which is more clear within the lower levels (**Fig. 9b**). As a result, consistent easterly  
365 anomalies appear from SWP to its northern flank around  $15^{\circ}\text{N}$ , denoting the active role of depressed air pressure. The  
366 consistent easterly anomalies over SWP could lead to local anticyclonic wind shear anomalies (Wang et al., 2019). In  
367 such a scenario, a quasi-barotropic SWPCGA can be induced (**Fig. 9c**). Further, local downward motions tied to SWPCGA  
368 could induce significant upward motions to its north via a meridional overturning circulation (J. Wang et al., 2021), thus  
369 exciting a quasi-barotropic cyclonic anomaly and an anticlockwise <WVT> gyre pattern centered over Northeast China  
370 (**Figs. 9a–c**). Therefore, positive summertime rainfall anomalies over EAMBZ at interdecadal timescales can be induced  
371 (**Fig. 9d**). Notably, circulation and precipitation anomalies during the warm phase years of the IOBM (**Fig. S5**) highly  
372 mirror those tied to the IOBM cooling with opposite signs.

### 373 374 **3.4 Results from CESM1 simulations**

375  
376 In this subsection, we use the pacemaker experimental data based on the ensemble mean of CESM1\_IOPES and  
377 CESM1\_LENS to validate our proposed mechanisms regarding the modulation of IOBM cooling on the interdecadal  
378 enhancement of summer EAMBZ precipitation. Considering the predominant role of southerly anomalies over the key  
379 monsoonal southerly domain, we therefore emphasize the low-level (850 hPa) atmospheric anomalies at interdecadal  
380 timescales tied to the IOBM-like SST cooling, as depicted in **Fig. 10**. We can observe a clearly anomalous cyclonic

381 circulation around the northeast corner of TIO, accompanied by local positive precipitation anomalies and easterly  
382 anomalies that stretch from SWP to its northern flank, which are generally resembled those in the observation (**Fig. 9**). In  
383 this circumstance, a similar “north-low–south-high” meridional seesaw pattern over the Northeast China–SWP sector can  
384 be simulated to spark and sustain the enhanced EAMBZ precipitation in boreal summer (**Fig. 10**). In summary, by and  
385 large, the ensemble mean composite results can well reproduce the observed anomalous circulation and precipitation  
386 driven by IOBM-related SSTAs, confirming the crucial role of IOBM cooling in driving enhanced summer precipitation  
387 over EAMBZ at interdecadal timescales.

388

### 389 **3.5 Estimation of the interdecadal variations of summer EAMBZ precipitation**

390

391 In the last three subsections, we suggest that the IOBM cooling can serve as a significant oceanic modulator for increased  
392 summer EAMBZ precipitation at interdecadal timescales based on observation evidences and pacemaker experiments,  
393 and present the corresponding physical mechanisms. To estimate their steady antiphase relationship, in the following, the  
394 negative  $I_{\text{IOBM}}$  is selected to construct a physical-based empirical model by using the simple linear regression analysis and  
395 the cross-validation method (You and Jia, 2018; Chang et al., 2021; Jeong et al., 2021), representing the impact of IOBM  
396 cooling. The physical-based model is given as follows:

397

$$398 I_{\text{EAMBZP}} = \beta_0 + \beta_1 I_{\text{IOBM}} + \varepsilon, \quad (5)$$

399

400 where  $\beta_0$  and  $\beta_1$  are regression coefficients, and  $\varepsilon$  denotes the residuals. The time series of  $I_{\text{EAMBZP}}$  and  $I_{\text{IOBM}}$  are detrended  
401 and 11-year low-pass filtered beforehand.

402

403 Following the method of Jeong et al. (2021), a “leaving one out” cross-validation strategy is employed to determine the  
404 robustness of the hindcast estimates. The normalized time series of summer  $I_{\text{EAMBZP}}$  and associated leave-one-out cross-  
405 validated hindcast estimates are shown in **Fig. 11**. The TCC between the physical-based predicted hindcast estimates (blue  
406 line) and the observed  $I_{\text{EAMBZP}}$  (red line) for 1901–2014 can reach 0.56 ( $P < 0.05$ ), suggesting that the physical-based  
407 model can well capture the interdecadal  $I_{\text{EAMBZP}}$  variations and reflect their steady relationship.

408

409 Although our proposed physical-based empirical model could confirm the concurrently intimately interdecadal  
410 relationship between IOBM and EAMBZ precipitation, we should acknowledge the shortcomings of the model.  
411 First, the amplitudes of the hindcast estimates are fairly lower, which cannot well capture the extreme precipitation  
412 years (e.g., years around 1960; **Fig. 11**). Second, the simultaneous signal of IOBM cannot be served as a predictor  
413 for summertime EAMBZ precipitation variations. As such, this model inherently lacks the ability to predict the  
414 interdecadal EAMBZ precipitation anomalies in advance.

415

## 416 **4 Conclusions and discussion**

417

418 In this study, by analysis of the long-term observational and reanalysis datasets during 1901–2014, the temporal  
419 characteristics of interdecadal variations in the summer EAMBZ precipitation and associated circulation background are  
420 revealed. The potential modulation of IOBM on the variations is further discussed. As a summary of our major findings,  
421 **Fig. 12** schematically synthesizes how IOBM-associated SST mode remotely drives the interdecadal precipitation  
422 fluctuations via a tropical route.

423

424 The summer EAMBZ precipitation exhibited a salient interdecadal fluctuations, e.g., with dry summers during the periods  
425 preceding 1927, 1939–1945, 1968–1982, and 1998–2010, as well as wet summers during the periods of 1928–1938,  
426 1946–1967, and 2011 onwards. It is indicated that the cold airflows brought by the mid-latitude accelerated upstream  
427 westerlies over the westerly-dominated domain collide and converge with the warm and humid airflows brought by the  
428 enhanced southerlies over the key EASM-controlled domain, suggesting the local extratropical–tropical interplay. Further  
429 diagnostic results suggest that the monsoonal southerly anomalies could be viewed as the predominant driving factor for  
430 the interdecadal enhancement of EAMBZ precipitation, whereas the upstream westerlies play a secondary dynamical  
431 amplification role. Such circulation anomalies are closely linked to a “north-low–south-high” meridional seesaw pattern  
432 over the Northeast China–SWP sector, which provides favorable environments for the transportation of water vapor from  
433 the SWP and the convergence over EAMBZ to spark enhanced summer EAMBZ precipitation at interdecadal timescales.

434  
435 We further identify that the IOBM-related SST anomaly pattern is a salient oceanic modulator for the interdecadal  
436 variations of the summer EAMBZ precipitation via the Gill–Matsuno mechanism. When the cold phase of the IOBM  
437 occurs, an anomalous cyclonic circulation is excited around the northeast corner of TIO in terms of the regional anti-  
438 symmetric atmospheric heating. As a response, consistent easterly anomalies appear from SWP to its northern flank,  
439 leading to local anticyclonic wind shear anomalies and thus inducing a SWPCGA pattern and a resultant anticlockwise  
440 gyre pattern centered over Northeast China. On interdecadal timescales, such meridional seesaw pattern tied to the IOBM  
441 cooling is responsible for enhanced summer precipitation over EAMBZ through linking the predominant driving factor  
442 of strengthened monsoonal southerly anomalies west of the SWPCGA pattern. As such, the water vapor transportation  
443 from the SWP and the convergence over EAMBZ can be triggered to induce and sustain the enhancement local  
444 precipitation. Correspondingly, a physical-based model based the negative  $I_{IOBM}$  is constructed, which can well capture  
445 the interdecadal fluctuations in the EAMBZ precipitation and reflect their steady relationship. Furthermore, the results  
446 based on the large ensemble experiment and the Indian Ocean pacemaker experiment also confirm the crucial physical  
447 pathway linking the SST variations over TIO with the summer precipitation over EAMBZ via the influence of SST  
448 variations on the aforementioned meridional seesaw pattern at interdecadal timescales.

449  
450 The following two points deserve further discussion. First, although results from CESM1\_LENS and CESM1\_IOPES  
451 can reasonably confirm our proposed physical pathway of how IOBM cooling exerts a distant modulation on the  
452 interdecadal enhancement of summer precipitation over EAMBZ, we can still notice the weakness of the model  
453 simulations. That is, positive precipitation anomalies around the northeast corner of TIO and the easterly anomalies  
454 exhibit weaker magnitudes compared to the observations (**Fig. 10** vs. **7b** and **9b**). Besides, systematic biases exist  
455 regarding the simulated positions of the upper (lower) tropospheric divergence (convergence) and negative (positive)  
456 RWS anomalies (**Fig. S6**), manifesting themselves in the eastward displacement tendency in contrast to those around the  
457 northeast corner of the TIO (**Fig. 8**).

458  
459 Second, this study merely identifies the physical linkage between the interdecadal summer EAMBZ precipitation  
460 and the contemporaneous SST mode over the TIO basin from the tropical route. Nonetheless, the contemporaneous  
461 IOBM is not a predictor. According to many previous studies (e.g., Wang et al., 2015; Li et al., 2023), the physical-  
462 based empirical model based on multiple predictors may better improve the forecast skill. Thus, it is urgent to find  
463 out more salient precursor signals of the lower boundary anomalies [e.g., sea ice (Han et al., 2021)] and figure out  
464 associated mechanisms for interdecadal EAMBZ precipitation changes to construct an effective prediction model.

465 **Code and data availability.** The CRU time series precipitation data version 3.26 (CRU TS3.26) from CRU at the  
466 University of East Anglia are available online (<https://catalogue.ceda.ac.uk/uuid/3f894480cc48e1cbc29a5ee12d8542d>;

467 CRU, 2022). The ERSSTv5 data from the US NOAA are available from the following website:  
468 <https://www1.ncdc.noaa.gov/pub/data/cmb/ersst/v5/netcdf/> (NOAA 2020). The 20CRv2c datasets from NOAA-CIRES  
469 are available from the following website: [https://psl.noaa.gov/data/gridded/data.20thC\\_ReanV2c.html](https://psl.noaa.gov/data/gridded/data.20thC_ReanV2c.html) (NOAA-CIRES,  
470 2022). The model simulation datasets regarding CESM1\_LENS are available online  
471 (<https://www.cesm.ucar.edu/community-projects/lens/data-sets>; NCAR 2023). The model simulation datasets regarding  
472 CESM1\_IOPEs are available online (<https://www.earthsystemgrid.org/dataset/ucar.cgd.cesm4.IOD-PACEMAKER.html>;  
473 NCAR 2023).

474 Codes are available from the corresponding author on reasonable request.

475

476 **Author contributions.** YL designed the research; JW wrote the first draft of the paper; FC and CS downloaded and  
477 analyzed the data, and plotted the figures used in this study. All authors, including YD and XX, contributed to the  
478 discussion of the results and reviewed the manuscript.

479

480 **Competing interests.** The contact author has declared that none of the authors has any competing interests.

481

482 **Acknowledgements.** Yanju Liu acknowledges the support by the Key Innovation Team of China Meteorological  
483 Administration “Climate Change Detection and Response” (CMA2022ZD03).

484

485 **Financial support.** This study was supported by the Second Tibetan Plateau Scientific Expedition and Research (STEP)  
486 program (2019QZKK010204-02 and 2019QZKK0102), Guangdong Major Project of Basic and Applied Basic Research  
487 (2020B0301030004), and Innovation and Development Special Project of China Meteorological Administration  
488 (CXFZ2022J039).

489

490

## 491 References

492

- 493 Chang, L., Wu, Z. and Xu, J., 2021. Contribution of Northeastern Asian stratospheric warming to subseasonal prediction  
494 of the early winter haze pollution in Sichuan Basin, China. *Science of the Total Environment*, 751: 141823.
- 495 Chen, F.-H., Chen, J.-H., Holmes, J., Boomer, I., Austin, P., Gates, J.B., Wang, N.-L., Brooks, S.J. and Zhang, J.-W., 2010.  
496 Moisture changes over the last millennium in arid central Asia: a review, synthesis and comparison with monsoon  
497 region. *Quaternary Science Reviews*, 29(7): 1055-1068.
- 498 Chen, J., Huang, W., Feng, S., Zhang, Q., Kuang, X., Chen, J. and Chen, F., 2021. The modulation of westerlies-monsoon  
499 interaction on climate over the monsoon boundary zone in East Asia. *International Journal of Climatology*,  
500 41(S1): E3049-E3064.
- 501 Chen, J., Huang, W., Jin, L., Chen, J., Chen, S. and Chen, F., 2018. A climatological northern boundary index for the East  
502 Asian summer monsoon and its interannual variability. *Science China Earth Sciences*, 61(1): 13-22.
- 503 Compo, G.P., Whitaker, J.S., Sardeshmukh, P.D., Matsui, N., Allan, R.J., Yin, X., Gleason, B.E., Vose, R.S., Rutledge, G.,  
504 Bessemoulin, P., Brönnimann, S., Brunet, M., Crouthamel, R.I., Grant, A.N., Groisman, P.Y., Jones, P.D., Kruk,  
505 M.C., Kruger, A.C., Marshall, G.J., Maugeri, M., Mok, H.Y., Nordli, Ø., Ross, T.F., Trigo, R.M., Wang, X.L.,  
506 Woodruff, S.D. and Worley, S.J., 2011. The Twentieth Century Reanalysis Project. *Quarterly Journal of the Royal  
507 Meteorological Society*, 137(654): 1-28.
- 508 CRU: CRU TS3.26, monthly, CRU [data set] <https://catalogue.ceda.ac.uk/uuid/3f8944800cc48e1cbc29a5ee12d8542d>,  
509 last access: 5 July 2022.
- 510 Ding, Y. and Chan, J.C.L., 2005. The East Asian summer monsoon: an overview. *Meteorology and Atmospheric Physics*,  
511 89(1): 117-142.
- 512 Dou, J. and Wu, Z., 2018. Southern Hemisphere origins for interannual variations of snow cover over the western Tibetan  
513 Plateau in boreal summer. *Journal of Climate*, 31(19): 7701-7718.
- 514 Duchon, C.E., 1979. Lanczos filtering in one and two dimensions. *Journal of Applied Meteorology and Climatology*,  
515 18(8): 1016-1022.

- 516 Gill, A.E., 1980. Some simple solutions for heat-induced tropical circulation. *Quarterly Journal of the Royal*  
517 *Meteorological Society*, 106(449): 447-462.
- 518 Han, T., Zhang, M., Zhu, J., Zhou, B. and Li, S., 2021. Impact of early spring sea ice in Barents Sea on midsummer  
519 rainfall distribution at Northeast China. *Climate Dynamics*, 57(3): 1023-1037.
- 520 Han, W., Vialard, J., McPhaden, M.J., Lee, T., Masumoto, Y., Feng, M. and de Ruijter, W.P.M., 2014. Indian Ocean  
521 decadal variability: A review. *Bulletin of the American Meteorological Society*, 95(11): 1679-1703.
- 522 Harris, I., Jones, P.D., Osborn, T.J. and Lister, D.H., 2014. Updated high-resolution grids of monthly climatic  
523 observations—the CRU TS3.10 Dataset. *International Journal of Climatology*, 34(3): 623-642.
- 524 Henley, B.J., Gergis, J., Karoly, D.J., Power, S., Kennedy, J. and Folland, C.K., 2015. A Tripole Index for the Interdecadal  
525 Pacific Oscillation. *Climate Dynamics*, 45(11): 3077-3090.
- 526 Huang, B., Thorne, P.W., Banzon, V.F., Boyer, T., Chepurin, G., Lawrimore, J.H., Menne, M.J., Smith, T.M., Vose, R.S.  
527 and Zhang, H.-M., 2017. Extended Reconstructed Sea Surface Temperature, version 5 (ERSSTv5): Upgrades,  
528 validations, and intercomparisons. *Journal of Climate*, 30(20): 8179-8205.
- 529 Huang, J., Li, Y., Fu, C., Chen, F., Fu, Q., Dai, A., Shinoda, M., Ma, Z., Guo, W., Li, Z., Zhang, L., Liu, Y., Yu, H., He,  
530 Y., Xie, Y., Guan, X., Ji, M., Lin, L., Wang, S., Yan, H. and Wang, G., 2017. Dryland climate change: Recent  
531 progress and challenges. *Reviews of Geophysics*, 55(3): 719-778.
- 532 Huang, J., Ma, J., Guan, X., Li, Y. and He, Y., 2019. Progress in semi-arid climate change studies in China. *Advances in*  
533 *Atmospheric Sciences*, 36(9): 922-937.
- 534 Huang, J., Zhang, G., Zhang, Y., Guan, X., Wei, Y. and Guo, R., 2020. Global desertification vulnerability to climate  
535 change and human activities. *Land Degradation & Development*, 31(11): 1380-1391.
- 536 Huang, W., Chen, J., Zhang, X., Feng, S. and Chen, F., 2015. Definition of the core zone of the “westerlies-dominated  
537 climatic regime”, and its controlling factors during the instrumental period. *Science China Earth Sciences*, 58(5):  
538 676-684.
- 539 Huang, Y., Wu, B., Li, T., Zhou, T. and Liu, B., 2019. Interdecadal Indian Ocean basin mode driven by interdecadal  
540 Pacific oscillation: A season-dependent growth mechanism. *Journal of Climate*, 32(7): 2057-2073.
- 541 Hurrell, J.W., Holland, M.M., Gent, P.R., Ghan, S., Kay, J.E., Kushner, P.J., Lamarque, J.F., Large, W.G., Lawrence, D.,  
542 Lindsay, K., Lipscomb, W.H., Long, M.C., Mahowald, N., Marsh, D.R., Neale, R.B., Rasch, P., Vavrus, S.,  
543 Vertenstein, M., Bader, D., Collins, W.D., Hack, J.J., Kiehl, J. and Marshall, S., 2013. The Community Earth  
544 System Model: A framework for collaborative research. *Bulletin of the American Meteorological Society*, 94(9):  
545 1339-1360.
- 546 Jeong, J.I., Park, R.J., Yeh, S.-W. and Roh, J.-W., 2021. Statistical predictability of wintertime PM<sub>2.5</sub> concentrations over  
547 East Asia using simple linear regression. *Science of the Total Environment*, 776: 146059.
- 548 Jiang, J., Zhou, T., Chen, X. and Wu, B., 2021. Central Asian precipitation shaped by the tropical Pacific decadal  
549 variability and the Atlantic multidecadal variability. *Journal of Climate*, 34(18): 7541-7553.
- 550 Kay, J.E., Deser, C., Phillips, A., Mai, A., Hannay, C., Strand, G., Arblaster, J.M., Bates, S.C., Danabasoglu, G., Edwards,  
551 J., Holland, M., Kushner, P., Lamarque, J.F., Lawrence, D., Lindsay, K., Middleton, A., Munoz, E., Neale, R.,  
552 Oleson, K., Polvani, L. and Vertenstein, M., 2015. The community earth system model (CESM) large ensemble  
553 project: a community resource for studying climate change in the presence of internal climate variability. *Bulletin*  
554 *of the American Meteorological Society*, 96(8): 1333-1349.
- 555 Klein, S.A., Soden, B.J. and Lau, N.-C., 1999. Remote sea surface temperature variations during ENSO: evidence for a  
556 tropical atmospheric bridge. *Journal of Climate*, 12(4): 917-932.
- 557 Li, J., Sun, C. and Jin, F.-F., 2013. NAO implicated as a predictor of Northern Hemisphere mean temperature multidecadal  
558 variability. *Geophysical Research Letters*, 40(20): 5497-5502.
- 559 Li, J. and Zeng, Q., 2002. A unified monsoon index. *Geophysical Research Letters*, 29(8): 115-1-115-4.
- 560 Li, J., Zheng, C., Yang, Y., Lu, R. and Zhu, Z., 2023. Predictability of spatial distribution of pre-summer extreme  
561 precipitation days over southern China revealed by the physical-based empirical model. *Climate Dynamics*,  
562 61(5): 2299-2316.
- 563 Li, M. and Ma, Z., 2018. Decadal changes in summer precipitation over arid northwest China and associated atmospheric  
564 circulations. *International Journal of Climatology*, 38(12): 4496-4508.
- 565 Lu, W. and Jia, G., 2013. Fluctuation of farming-pastoral ecotone in association with changing East Asia monsoon climate.  
566 *Climatic Change*, 119(3): 747-760.
- 567 Mastyo, M., 2013. Bilinear interpolation theorems and applications. *Journal of Functional Analysis*, 265(2): 185-207.
- 568 Matsuno, T., 1966. Quasi-geostrophic motions in the equatorial area. *Journal of the Meteorological Society of Japan*,  
569 44(1): 25-43.
- 570 Moss, R.H., Edmonds, J.A., Hibbard, K.A., Manning, M.R., Rose, S.K., van Vuuren, D.P., Carter, T.R., Emori, S.,

571 Kainuma, M., Kram, T., Meehl, G.A., Mitchell, J.F.B., Nakicenovic, N., Riahi, K., Smith, S.J., Stouffer, R.J.,  
572 Thomson, A.M., Weyant, J.P. and Wilbanks, T.J., 2010. The next generation of scenarios for climate change  
573 research and assessment. *Nature*, 463(7282): 747-756.

574 NCAR: CESM1\_LENS, monthly, NCAR [data set] <https://www.cesm.ucar.edu/community-projects/lens/data-sets>, last  
575 access: 28 April 2023.

576 NCAR: CESM1\_IOPES, monthly, NCAR [data set] [https://www.earthsystemgrid.org/dataset/ucar.cgd.cesm4.IOD-  
577 PACEMAKER.html](https://www.earthsystemgrid.org/dataset/ucar.cgd.cesm4.IOD-PACEMAKER.html), last access: 4 May 2023.

578 NOAA: ERSSTv5, monthly, NOAA [data set] <https://www1.ncdc.noaa.gov/pub/data/cmb/ersst/v5/netcdf/>, last access: 15  
579 October 2020.

580 NOAA-CIRES: 20CRv2c, monthly, NOAA-CIRES [data set]  
581 [https://psl.noaa.gov/data/gridded/data.20thC\\_ReanV2c.html](https://psl.noaa.gov/data/gridded/data.20thC_ReanV2c.html), last access: 26 June 2022.

582 North, G.R., Bell, T.L., Cahalan, R.F. and Moeng, F.J., 1982. Sampling errors in the estimation of empirical orthogonal  
583 functions. *Monthly Weather Review*, 110(7): 699-706.

584 Ou, T.H. and Qian, W.H., 2006. Vegetation variations along the monsoon boundary zone in East Asia. *Chinese Journal of  
585 Geophysics (in Chinese)*, 49(3): 698–705.

586 Piao, J., Chen, W. and Chen, S., 2021. Water vapour transport changes associated with the interdecadal decrease in the  
587 summer rainfall over Northeast Asia around the late-1990s. *International Journal of Climatology*, 41(S1): E1469-  
588 E1482.

589 Qian, W., Ding, T., Hu, H., Lin, X. and Qin, A., 2009. An overview of dry-wet climate variability among monsoon-  
590 westerly regions and the monsoon northernmost marginal active zone in China. *Advances in Atmospheric  
591 Sciences*, 26(4): 630-641.

592 Sardeshmukh, P.D. and Hoskins, B.J., 1988. The generation of global rotational flow by steady idealized tropical  
593 divergence. *Journal of Atmospheric Sciences*, 45(7): 1228-1251.

594 Schiemann, R., Lüthi, D. and Schär, C., 2009. Seasonality and interannual variability of the westerly jet in the Tibetan  
595 Plateau region. *Journal of Climate*, 22(11): 2940-2957.

596 Si, D. and Ding, Y., 2016. Oceanic forcings of the interdecadal variability in East Asian summer rainfall. *Journal of  
597 Climate*, 29(21): 7633-7649.

598 Si, D., Jiang, D., Hu, A. and Lang, X., 2021. Variations in northeast Asian summer precipitation driven by the Atlantic  
599 multidecadal oscillation. *International Journal of Climatology*, 41(3): 1682-1695.

600 Song, C., Wang, J., Liu, Y., Zhang, L., Ding, Y., Li, Q., Shen, X., Song, Y. and Yan, Y., 2022. Toward role of westerly-  
601 monsoon interplay in linking interannual variations of late spring precipitation over the southeastern Tibetan  
602 Plateau. *Atmospheric Science Letters*, 23(3): e1074.

603 Sun, B., Li, H. and Zhou, B., 2019a. Interdecadal variation of Indian Ocean basin mode and the impact on Asian summer  
604 climate. *Geophysical Research Letters*, 46(21): 12388-12397.

605 Sun, B., Wang, H., Zhou, B. and Li, H., 2019b. Interdecadal variation in the synoptic features of mei-yu in the Yangtze  
606 River valley region and relationship with the Pacific decadal oscillation. *Journal of Climate*, 32(19): 6251-6270.

607 Taylor, K.E., Stouffer, R.J. and Meehl, G.A., 2012. An overview of CMIP5 and the experiment design. *Bulletin of the  
608 American Meteorological Society*, 93(4): 485-498.

609 Touma, D., Stevenson, S., Lehner, F. and Coats, S., 2021. Human-driven greenhouse gas and aerosol emissions cause  
610 distinct regional impacts on extreme fire weather. *Nature Communications*, 12(1): 212.

611 Wang, B., Wu, Z., Li, J., Liu, J., Chang, C.-P., Ding, Y. and Wu, G., 2008. How to measure the strength of the East Asian  
612 summer monsoon. *Journal of Climate*, 21(17): 4449-4463.

613 Wang, B., Xiang, B., Li, J., Webster, P.J., Rajeevan, M.N., Liu, J. and Ha, K.-J., 2015. Rethinking Indian monsoon rainfall  
614 prediction in the context of recent global warming. *Nature Communications*, 6(1): 7154.

615 Wang, J., Zhu, Z.W., Qi, L., Zhao, Q.H., He, J.H. and Wang, J.X.L., 2019. Two pathways of how remote SST anomalies  
616 drive the interannual variability of autumnal haze days in the Beijing–Tianjin–Hebei region, China. *Atmospheric  
617 Chemistry and Physics*, 19(3): 1521-1535.

618 Wang, J., Liu, Y., Ding, Y. and Wu, Z., 2021. Towards influence of Arabian Sea SST anomalies on the withdrawal date of  
619 Meiyu over the Yangtze-Huaihe River basin. *Atmospheric Research*, 249: 105340.

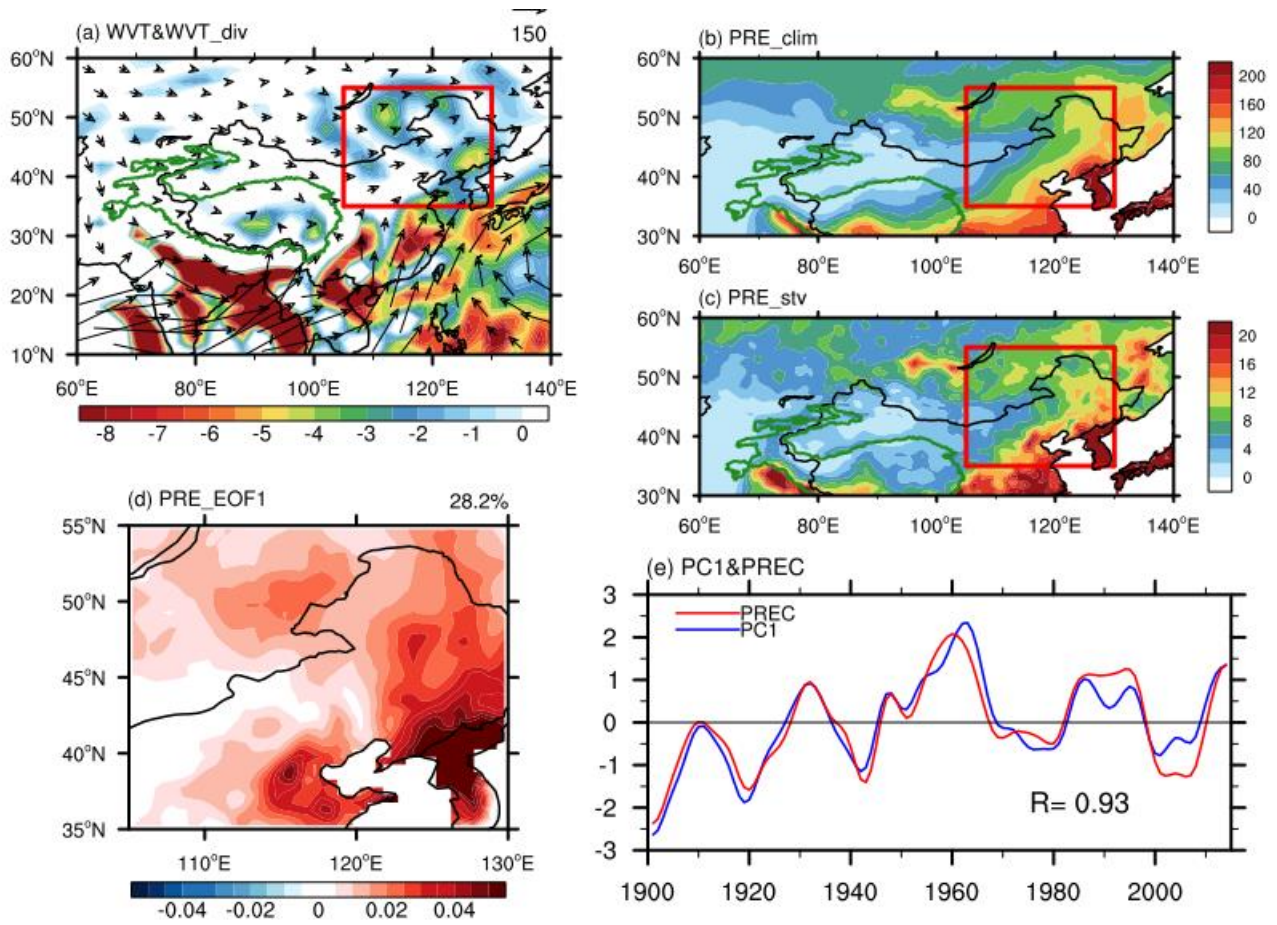
620 Wang, J., Liu, Y., Song, C., Ding, Y., Li, Q., Wu, P., Xu, Y. and Xu, X., 2022. Synergistic impacts of westerlies and  
621 monsoon on interdecadal variations of late spring precipitation over the southeastern extension of the Tibetan  
622 Plateau. *International Journal of Climatology*, 42(14): 7342-7361.

623 Wang, J., Liu, Y., Yang, Y., Wu, P., Yang, J., Liang, P., Song, C., Zhang, S. and Ding, Y., 2023. Impact of early winter  
624 North Atlantic Oscillation on the dramatic alternation of seesaw haze intensity between late winter months in  
625 the North China Plain. *Atmospheric Research*, 281: 106483.

- 626 Wang, L., Chen, W., Huang, G. and Zeng, G., 2017. Changes of the transitional climate zone in East Asia: past and future.  
627 *Climate Dynamics*, 49(4): 1463-1477.
- 628 Wang, Q., Wang, L., Huang, G., Piao, J. and Chotamonsak, C., 2021. Temporal and spatial variation of the transitional  
629 climate zone in summer during 1961–2018. *International Journal of Climatology*, 41(3): 1633-1648.
- 630 Wang, Q., Wang, L., Huang, G. and Wang, T., 2022. Mechanism of the summer rainfall interannual variability in  
631 transitional climate zone in East Asia: roles of teleconnection patterns and associated moisture processes.  
632 *Climate Dynamics*, <https://doi.org/10.1007/s00382-022-06618-1>.
- 633 Wang, Q., Huang, G., Wang, L., Piao, J., Ma, T., Hu, P., Chotamonsak, C. and Limsakul, A., 2023. Mechanism of the  
634 summer rainfall variation in Transitional Climate Zone in East Asia from the perspective of moisture supply  
635 during 1979–2010 based on the Lagrangian method. *Climate Dynamics*, 60(3): 1225-1238.
- 636 Wang, S., Huang, J., Huang, G., Luo, F., Ren, Y. and He, Y., 2022. Enhanced impacts of Indian Ocean sea surface  
637 temperature on the dry/wet variations over Northwest China. *Journal of Geophysical Research: Atmospheres*,  
638 127(11): e2022JD036533.
- 639 Wu, B., Zhou, T. and Li, T., 2016. Impacts of the Pacific–Japan and circumglobal teleconnection patterns on the  
640 interdecadal variability of the East Asian summer monsoon. *Journal of Climate*, 29(9): 3253-3271.
- 641 Wu, G., Guan, Y., Liu, Y., Yan, J. and Mao, J., 2012. Air–sea interaction and formation of the Asian summer monsoon  
642 onset vortex over the Bay of Bengal. *Climate Dynamics*, 38(1): 261-279.
- 643 Wu, P., Liu, Y., Ding, Y., Li, X. and Wang, J., 2022. Modulation of sea surface temperature over the North Atlantic and  
644 Indian-Pacific warm pool on interdecadal change of summer precipitation over northwest China. *International  
645 Journal of Climatology*, 42(16): 8526-8538.
- 646 Xie, S.-P., Hu, K., Hafner, J., Tokinaga, H., Du, Y., Huang, G. and Sampe, T., 2009. Indian Ocean capacitor effect on  
647 Indo–western Pacific climate during the summer following El Niño. *Journal of Climate*, 22(3): 730-747.
- 648 Xing, W. and Wang, B., 2017. Predictability and prediction of summer rainfall in the arid and semi-arid regions of China.  
649 *Climate Dynamics*, 49(1): 419-431.
- 650 Yang, D., Arblaster, J.M., Meehl, G.A., England, M.H., Lim, E.-P., Bates, S. and Rosenbloom, N., 2020. Role of tropical  
651 variability in driving decadal shifts in the Southern Hemisphere summertime eddy-driven jet. *Journal of Climate*,  
652 33(13): 5445-5463.
- 653 Yang, J., Liu, Q., Xie, S.-P., Liu, Z. and Wu, L., 2007. Impact of the Indian Ocean SST basin mode on the Asian summer  
654 monsoon. *Geophysical Research Letters*, 34(2): L02708.
- 655 Yeh, T.-C., Dao, S.-Y. and Li, M.-T., 1959. The abrupt change of circulation over the Northern Hemisphere during June  
656 and October. *The Atmosphere and the Sea in Motion*, the Rockefeller Institute Press and Oxford University Press,  
657 249-267.
- 658 Ying, K., Jiang, D., Zheng, X., Frederiksen, C.S., Peng, J., Zhao, T. and Zhong, L., 2023. Seasonal predictable source of  
659 the East Asian summer monsoon rainfall in addition to the ENSO–AO. *Climate Dynamics*, 60(7): 2459-2480.
- 660 You, Y. and Jia, X., 2018. Interannual variations and prediction of spring precipitation over China. *Journal of Climate*,  
661 31(2): 655-670.
- 662 Zeng, J. and Zhang, Q., 2019. A humidity index for the summer monsoon transition zone in East Asia. *Climate Dynamics*,  
663 53(9): 5511-5527.
- 664 Zhang, L., Han, W., Karnauskas, K.B., Meehl, G.A., Hu, A., Rosenbloom, N. and Shinoda, T., 2019. Indian Ocean  
665 warming trend reduces Pacific warming response to anthropogenic greenhouse gases: An interbasin thermostat  
666 mechanism. *Geophysical Research Letters*, 46(19): 10882-10890.
- 667 Zhang, Z., Sun, X. and Yang, X.-Q., 2018. Understanding the interdecadal variability of East Asian summer monsoon  
668 precipitation: Joint influence of three oceanic signals. *Journal of Climate*, 31(14): 5485-5506.
- 669 Zhao, W., Chen, S., Chen, W., Yao, S., Nath, D. and Yu, B., 2019a. Interannual variations of the rainy season withdrawal  
670 of the monsoon transitional zone in China. *Climate Dynamics*, 53(3): 2031-2046.
- 671 Zhao, W., Chen, W., Chen, S., Yao, S.-L. and Nath, D., 2019b. Inter-annual variations of precipitation over the monsoon  
672 transitional zone in China during August–September: Role of sea surface temperature anomalies over the  
673 tropical Pacific and North Atlantic. *Atmospheric Science Letters*, 20(1): e872.
- 674 Zhao, W., Chen, W., Chen, S., Nath, D. and Wang, L., 2020. Interdecadal change in the impact of North Atlantic SST on  
675 August rainfall over the monsoon transitional belt in China around the late 1990s. *Theoretical and Applied  
676 Climatology*, 140(1): 503-516.

677  
678  
679

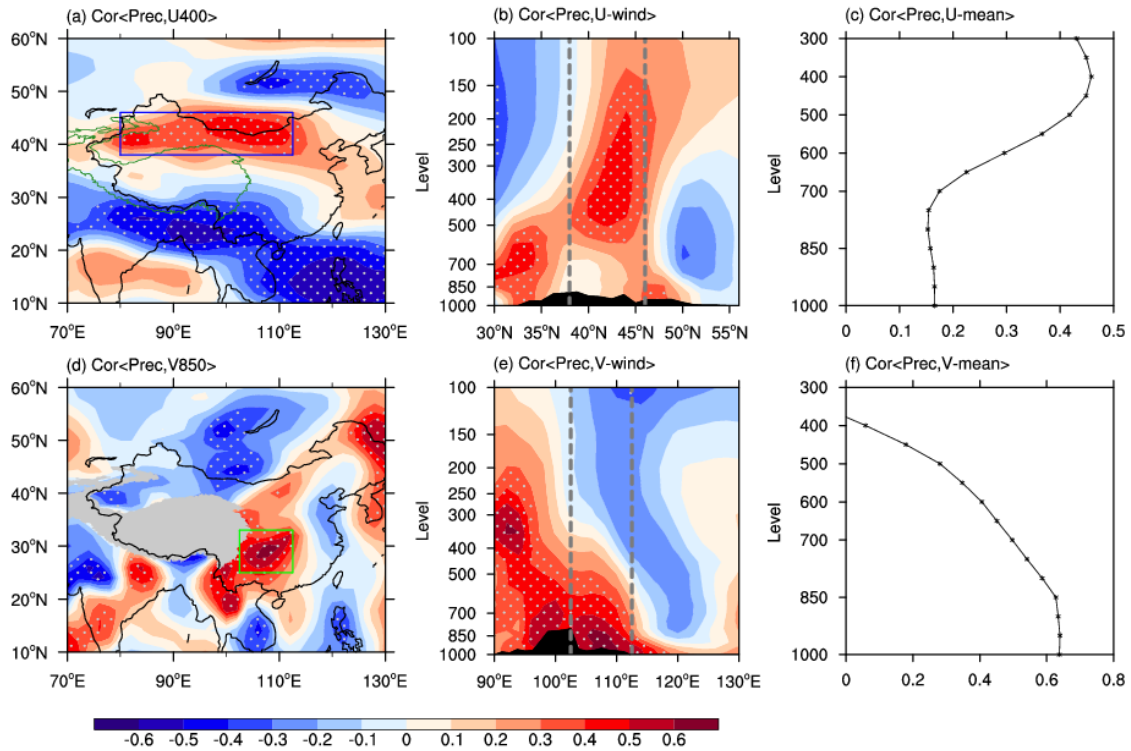
680 **Figures**  
 681



682  
 683 **Figure 1.** The climatological JJA-averaged (a)  $\langle WVT \rangle$  (vectors;  $\text{kg m}^{-1} \text{s}^{-1}$ ) and  $\langle WVT\_div \rangle$  (shading;  $10^{-5} \text{ kg m}^{-2} \text{ s}^{-1}$ ), (b)  
 684 precipitation ( $\text{mm month}^{-1}$ ), and (c) interdecadal standard deviation of precipitation ( $\text{mm month}^{-1}$ ) during the period 1901–2014. The  
 685 red box ( $35^{\circ}$ – $55^{\circ}\text{N}$ ,  $105^{\circ}$ – $130^{\circ}\text{E}$ ) outlines the research domain of EAMBZ (the same hereinafter). (d) Spatial pattern of the first  
 686 empirical orthogonal function (EOF1) mode of JJA-mean EAMBZ precipitation. (e) Normalized time series of the JJA-mean EAMBZ  
 687 precipitation index ( $I_{EAMBZP}$ ) (red line) and associated first principal component (PC1) (blue line), with the number denoting the  
 688 temporal correlation coefficient (TCC) between the corresponding time series. In panels (c)–(e), variables are detrended and 11-year  
 689 low-pass filtered. The green outline in panels (a)–(c) represents the terrain of the Tibetan Plateau (TP) at 2000 m (the same hereinafter).  
 690 The precipitation is derived from the CRU TS3.26 precipitation data, while other variables are from the 20CRv2c datasets.

691  
 692  
 693  
 694  
 695





696

697

698

699

700

701

702

703

704

705

706

707

708

709

710

711

712

713

714

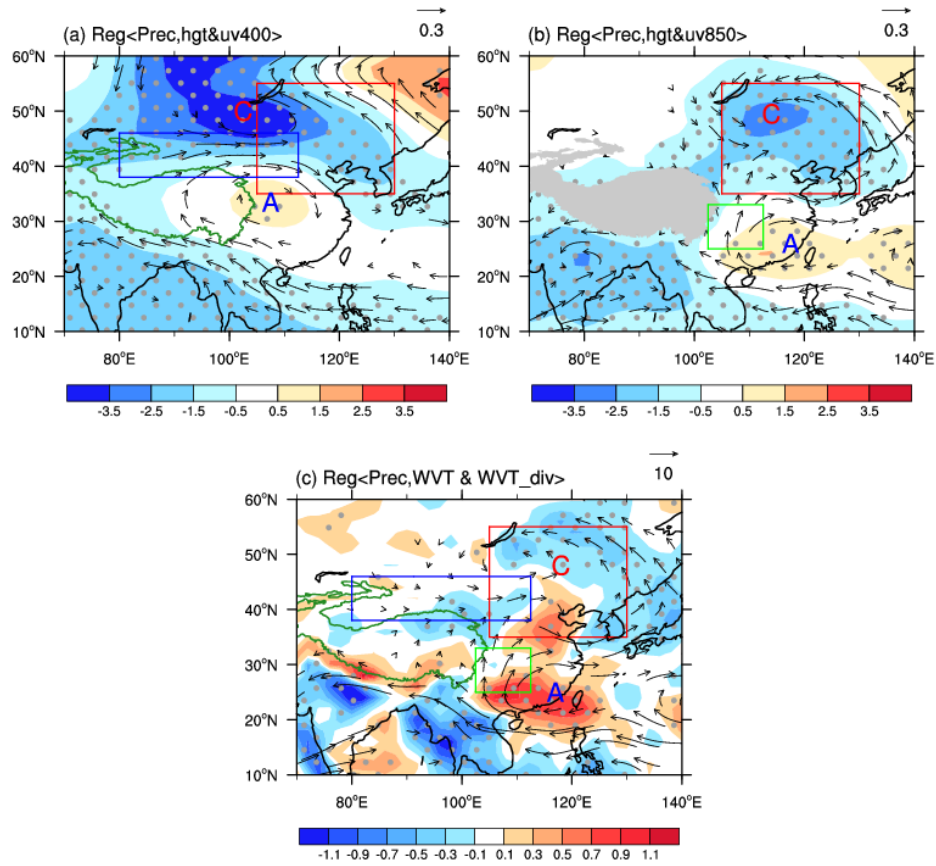
715

716

717

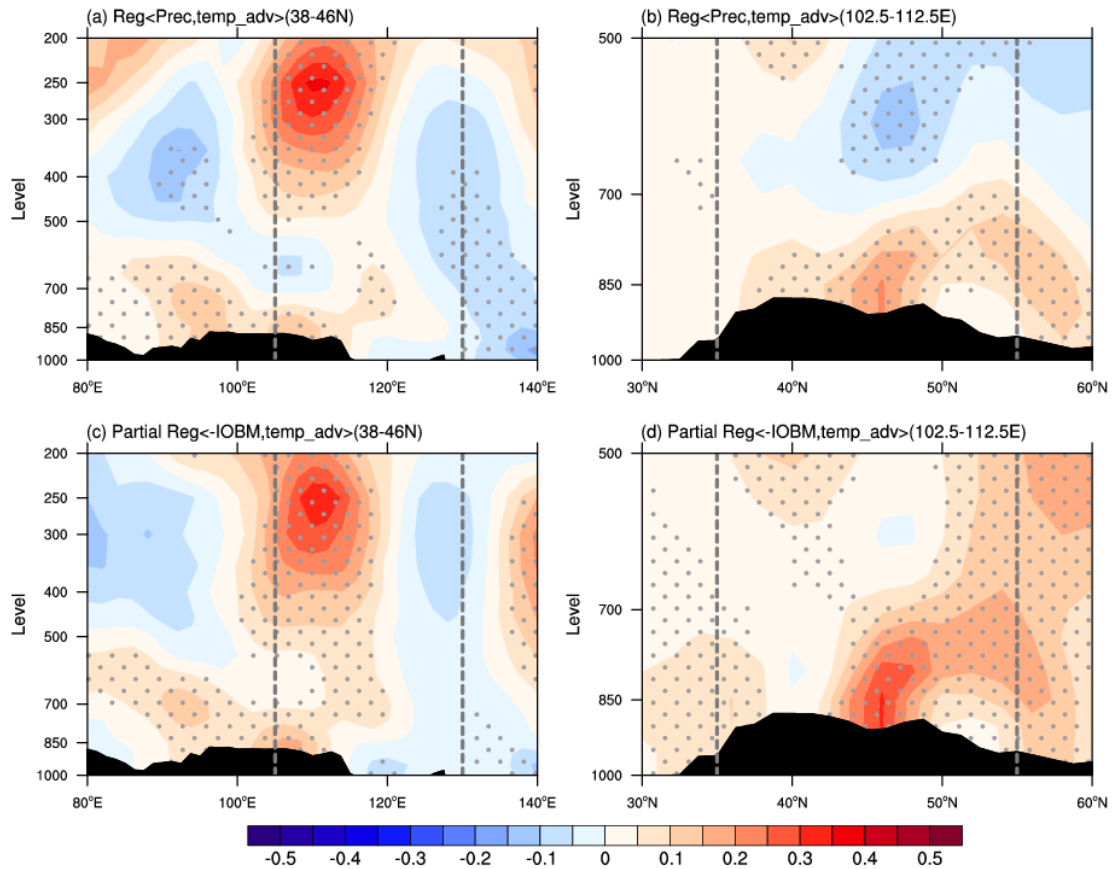
718

**Figure 2.** Correlation maps of the JJA-averaged  $I_{EAMBZP}$  with the simultaneous (a) 400-hPa zonal wind and (d) 850-hPa meridional wind, and (b) height–latitude cross-section of zonal winds averaged over  $80^{\circ}$ – $112.5^{\circ}$ E, and (e) height–longitude cross-section of meridional winds averaged over  $25^{\circ}$ – $33^{\circ}$ N, during the period 1901–2014. The blue box ( $38^{\circ}$ – $46^{\circ}$ N,  $80^{\circ}$ – $112.5^{\circ}$ E) in (a) and the green box ( $25^{\circ}$ – $33^{\circ}$ N,  $102.5^{\circ}$ – $112.5^{\circ}$ E) in (d) represent the upstream westerly domain and the monsoonal southerly domain significantly tied to the interdecadal variations of precipitation over EAMBZ, respectively (the same hereinafter). The grey-dashed vertical lines in (b) and (e) represent the latitudinal and longitudinal range of the westerly and the monsoonal southerly domain, respectively. (c) Profile of correlation coefficients between the JJA-averaged  $I_{EAMBZP}$  and the simultaneous area-averaged zonal winds over the upstream westerly domain at multiple levels during the period 1901–2014. (f) As in (c), but for the meridional winds over the monsoonal southerly domain. All variables are detrended and 11-year low-pass filtered. Areas with significant values exceeding the 95% confidence level are stippled. The black shading indicates the topography. The grey shaded areas denote the TP areas above 2000 m (the same hereinafter). The  $I_{EAMBZP}$  is calculated based on the CRU TS3.26 precipitation data, while other variables are from the 20CRv2c datasets.



719  
 720 **Figure 3.** Regression maps of the JJA-mean anomalies of (a) 400-hPa geopotential height (Z400; shading; m) and wind field (UV400;  
 721 vectors;  $\text{m s}^{-1}$ ), (b) 850-hPa geopotential height (Z850; shading; m) and wind field (UV850; vectors;  $\text{m s}^{-1}$ ), and (c)  $\langle \text{WVT} \rangle$  (vectors;  
 722  $\text{kg m}^{-1} \text{s}^{-1}$ ) and  $\langle \text{WVT}_{\text{div}} \rangle$  (shading;  $10^{-5} \text{ kg m}^{-2} \text{s}^{-1}$ ) onto the concurrent  $I_{\text{EAMBZP}}$  during the period 1901–2014. All variables are  
 723 detrended and 11-year low-pass filtered. Letter A (C) represents the center of anticyclonic (cyclonic) anomaly (the same hereinafter).  
 724 Areas with significant values of Z400, Z850, and  $\langle \text{WVT}_{\text{div}} \rangle$  that exceed the 95% confidence level are stippled, respectively. Only  
 725 vectors that are significant at the 95% confidence level are shown. The  $I_{\text{EAMBZP}}$  is calculated based on the CRU TS3.26 precipitation  
 726 data, while other variables are from the 20CRv2c datasets.

727  
 728  
 729  
 730  
 731  
 732  
 733  
 734  
 735  
 736  
 737  
 738  
 739



740

741

742

743

744

745

746

747

748

749

750

751

752

753

754

755

756

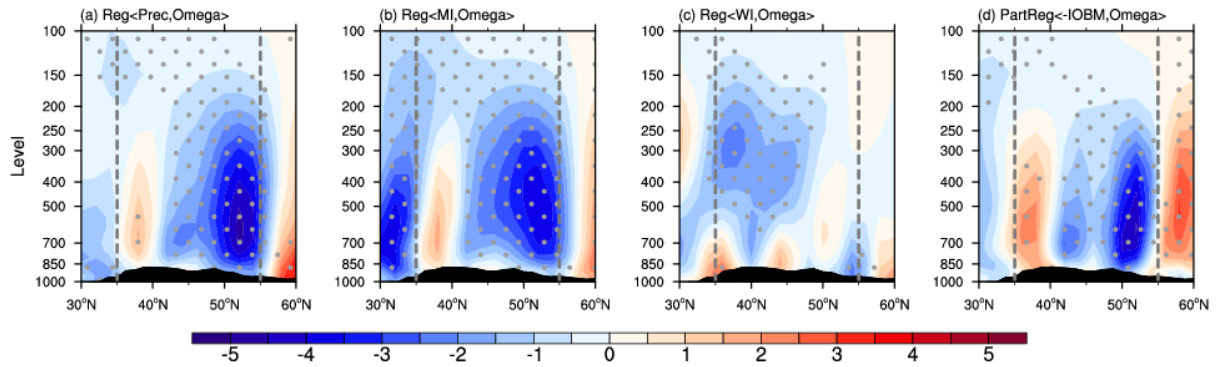
757

758

759

760

**Figure 4.** (a) Height–longitude cross-section (averaged over 38°–46°N) and (b) height–latitude cross-section (averaged over 102.5°–112.5°E) of the JJA-mean temperature advection anomalies (shading;  $10^{-5} \text{ K s}^{-1}$ ) regressed onto the concurrent  $I_{EAMBZP}$  during the period 1901–2014. (c, d) As in (a, b), but for patterns of the partial regression coefficient between temperature advection and negative  $I_{IOBM}$  without the IPO signal. The gray vertical lines in (a, c) and (b, d) represent the longitudinal and latitudinal range of the research domain of EAMBZ, respectively. The black shading indicates the topography. All variables are detrended and 11-year low-pass filtered. Areas with significant values exceeding the 95% confidence level are stippled. The  $I_{EAMBZP}$  and  $I_{IOBM}/\text{IPO}$  index are calculated based on the CRU TS3.26 precipitation data and the ERSSTv5 dataset, respectively; whilst other variables are from the 20CRv2c datasets.



761

762 **Figure 5.** Height–latitude cross-section (averaged over 105°–130°E) of the JJA-mean vertical velocity anomalies ( $10^{-3} \text{Pa s}^{-1}$ ) regressed  
 763 onto the concurrent (a)  $I_{\text{EAMBZP}}$ , (b)  $I_{\text{MI}}$ , and (c)  $I_{\text{WI}}$  during the period 1901–2014. (d) As in (a), but for the partial regressed anomalies  
 764 onto the negative  $I_{\text{IOBM}}$  with the IPO signal removed. The gray vertical lines represent the latitudinal range of EAMBZ. The black  
 765 shading indicates the topography. All variables are detrended and 11-year low-pass filtered. Areas with significant values exceeding  
 766 the 95% confidence level are stippled. The  $I_{\text{EAMBZP}}$  and  $I_{\text{IOBM/IPO}}$  index are calculated based on the CRU TS3.26 precipitation data  
 767 and the ERSSTv5 dataset, respectively; whilst other variables are from the 20CRv2c datasets.

768

769

770

771

772

773

774

775

776

777

778

779

780

781

782

783

784

785

786

787

788

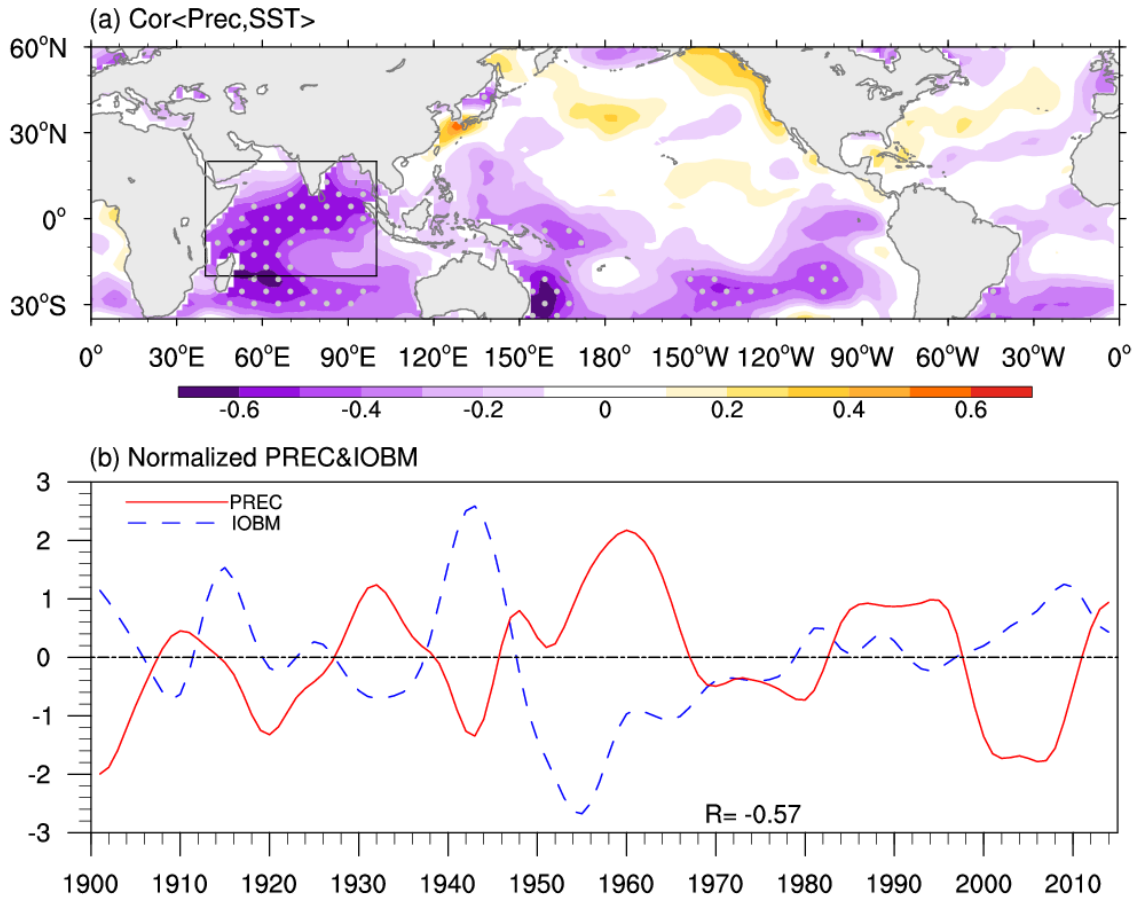
789

790

791

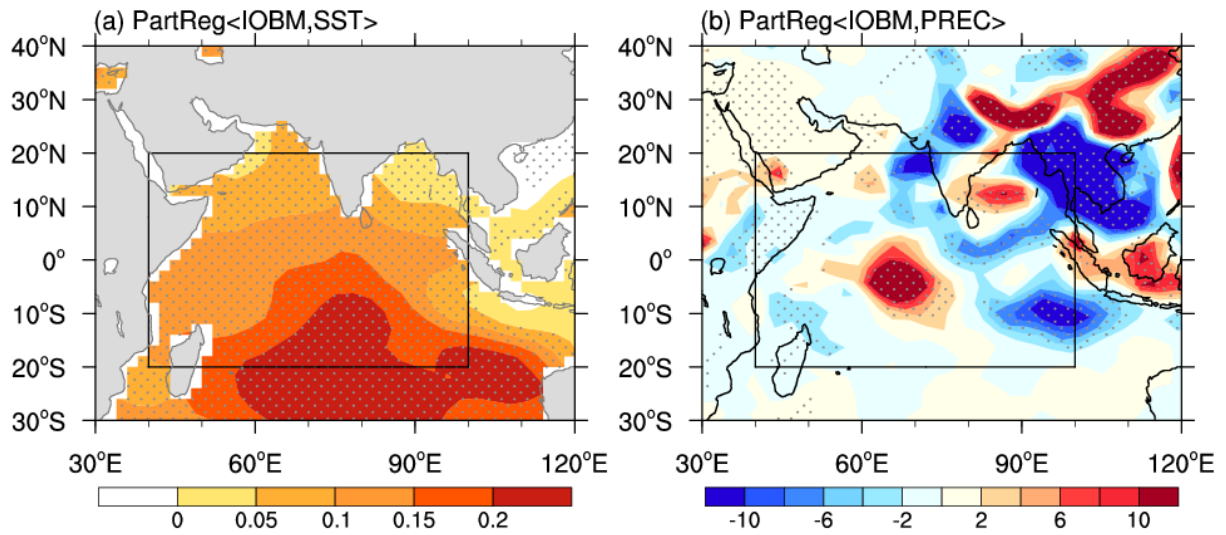
792

793



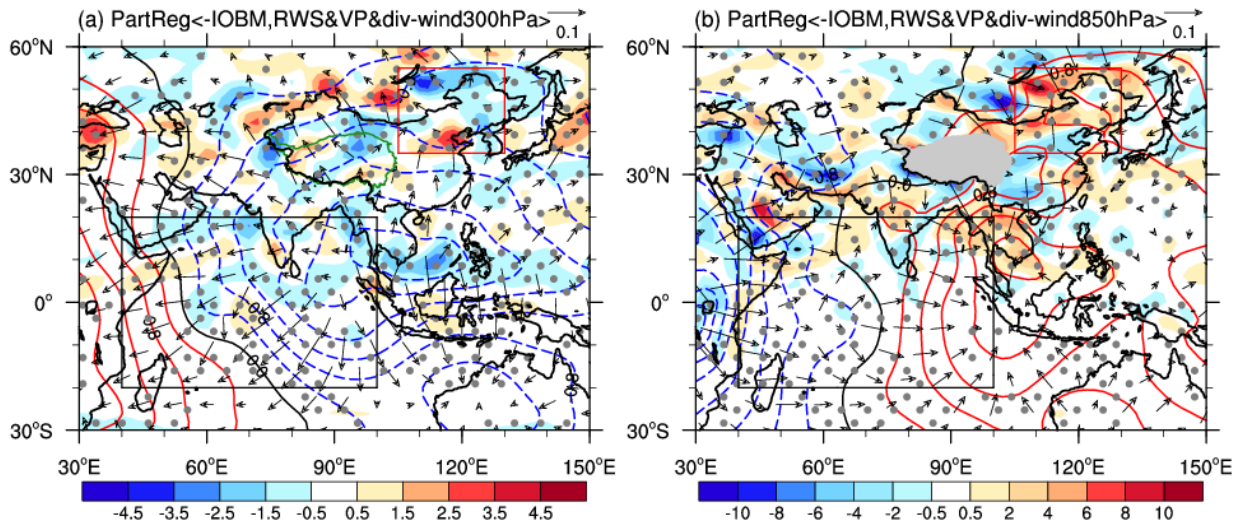
794  
 795 **Figure 6.** (a) Correlation map of the JJA-mean  $I_{EAMBZP}$  with the concurrent near-global SST (35°S–60°N) during the period 1901–  
 796 2014. The black frame (20°S–20°N, 40°–100°E) outlines the domain for delineating the IOBM mode (the same hereinafter). Areas  
 797 with significant values exceeding the 99% confidence level are stippled. (b) Normalized time series of the JJA-mean  $I_{EAMBZP}$  (red line)  
 798 and  $I_{IOBM}$  (blue line) from 1901 to 2014. The numeral at the bottom represents the TCC between the corresponding time series. All  
 799 variables are detrended and 11-year low-pass filtered. The SST is from the ERSSTv5 dataset. The  $I_{EAMBZP}$  and  $I_{IOBM}$  are calculated  
 800 based on the CRU TS3.26 precipitation data and the ERSSTv5 datasets, respectively.

801  
 802  
 803  
 804  
 805  
 806  
 807  
 808  
 809  
 810  
 811  
 812  
 813



814  
 815 **Figure 7.** Partial regression of the JJA-mean (a) SST (°C) and (b) precipitation (mm month<sup>-1</sup>) anomalies over TIO and its neighboring  
 816 areas onto the concurrent  $I_{IOBM}$  with the IPO signal removed for the period 1901–2014. All variables are detrended and 11-year low-  
 817 pass filtered. Areas with significant values exceeding the 95% confidence level are stippled. The  $I_{IOBM}$ /IPO index is calculated based  
 818 on the ERSSTv5 dataset. The SST and the precipitation are derived from the ERSSTv5 dataset and the 20CRv2c dataset, respectively.

819  
 820  
 821  
 822  
 823  
 824  
 825  
 826  
 827  
 828  
 829  
 830  
 831  
 832  
 833  
 834  
 835



836

837

838

839

840

841

842

843

844

845

846

847

848

849

850

851

852

853

854

855

856

857

858

859

860

861

862

863

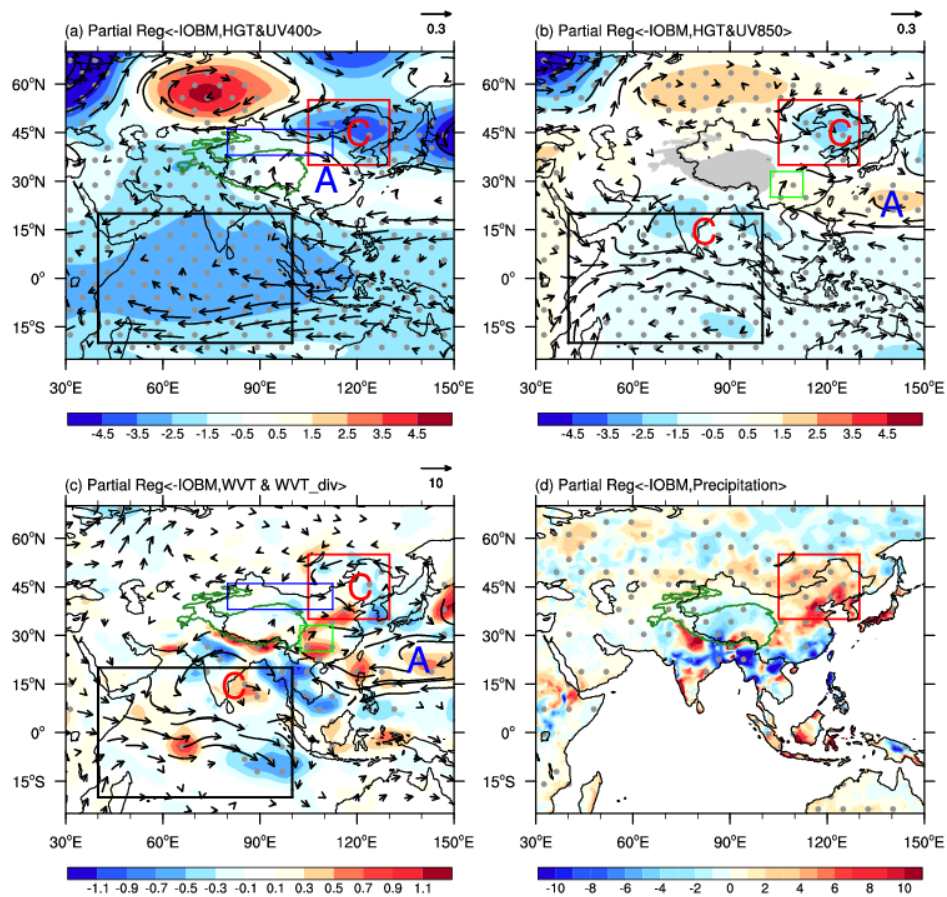
864

865

866

867

**Figure 8.** Partial regression of the JJA-mean (a) 300- and (b) 850-hPa RWS (shading;  $10^{-11} \text{ s}^{-2}$ ), velocity potential (contours; interval:  $0.4; 10^5 \text{ m}^2 \text{ s}^{-1}$ ), and divergent horizontal wind (vectors;  $\text{m s}^{-1}$ ) anomalies against the concurrent negative  $I_{\text{IOBM}}$  with the IPO signal removed during the period 1901–2014. All variables are detrended and 11-year low-pass filtered. Areas with significant values of RWS exceeding the 95% confidence level are stippled. The  $I_{\text{IOBM}}$ /IPO index is calculated based on the ERSSTv5 dataset; whilst other variables are from the 20CRv2c datasets.



868

869

870

871

872

873

874

875

876

877

878

879

880

881

882

883

884

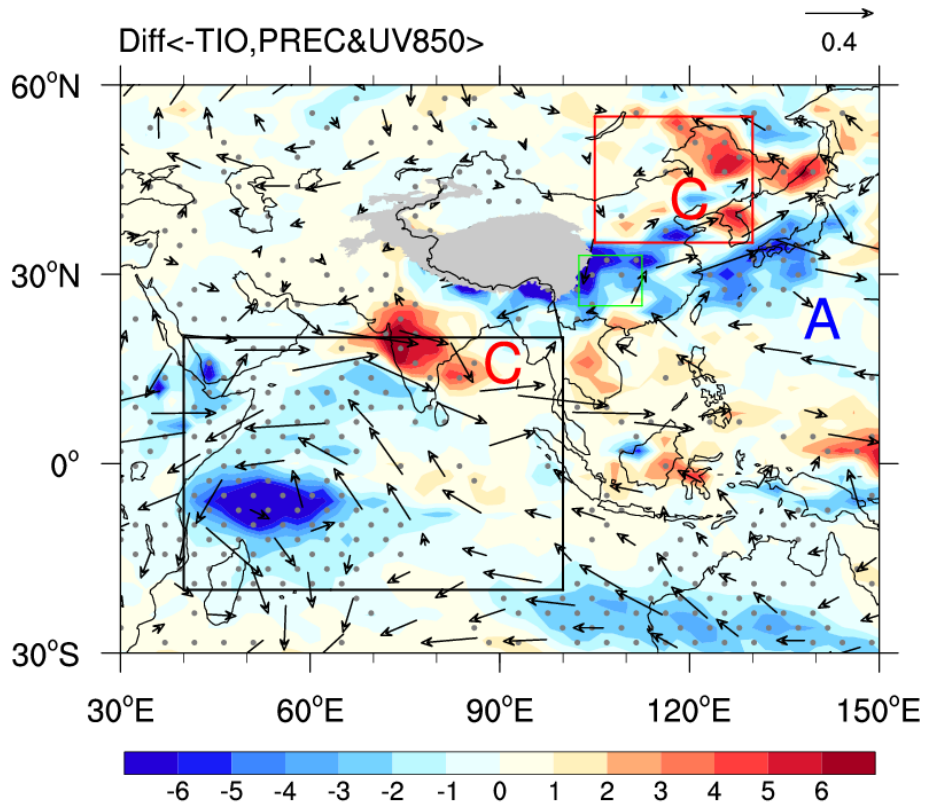
885

886

887

**Figure 9.** Partial regression of the JJA-mean (a) Z400 (shading; m) and UV400 (vectors;  $\text{m s}^{-1}$ ), (b) Z850 (shading; m) and UV850 (vectors;  $\text{m s}^{-1}$ ), (c)  $\langle \text{WVT} \rangle$  (vectors;  $\text{kg m}^{-1} \text{s}^{-1}$ ) and  $\langle \text{WVT}_{\text{div}} \rangle$  (shading;  $10^{-5} \text{kg m}^{-2} \text{s}^{-1}$ ), and precipitation ( $\text{mm month}^{-1}$ ) anomalies onto the concurrent negative  $I_{\text{IOBM}}$  with the IPO signal removed during the period 1901–2014. All variables are detrended and 11-year low-pass filtered. Areas with significant values of Z400, Z850, and  $\langle \text{WVT}_{\text{div}} \rangle$  that exceed the 95% confidence level are stippled, respectively. Only vectors that are significant at the 95% confidence level are shown. The  $I_{\text{IOBM}}$ /IPO index is calculated based on the ERSSTv5 dataset; the precipitation is derived from the CRU TS3.26 precipitation data; whilst other variables are from the 20CRv2c datasets.





888

889 **Figure 10.** Simulated composite differences of JJA-mean UV850 (vectors;  $\text{m s}^{-1}$ ) and precipitation (shading;  $\text{mm month}^{-1}$ ) between  
 890 cold and warm SST years over the broader TIO domain in CESM1\_IOPES ( $15^{\circ}\text{S}$ – $15^{\circ}\text{N}$ ,  $40^{\circ}$ – $174^{\circ}\text{E}$ ; purple box in **Fig. S4**). The warm  
 891 and cold TIO SST years are selected based on the  $\pm 0.5$  standard deviations of the simulated time-evolving SSTAs during 1920–2005,  
 892 as shown in **Fig. S3** (red line). All variables are detrended and 11-year low-pass filtered. Areas with significant values of precipitation  
 893 that exceed the 95% confidence level are stippled. Only vectors that are significant at the 95% confidence level are shown. The  
 894 simulated anomalies of UV850 and precipitation are calculated based on the difference between the CESM1\_IOPES ensemble mean  
 895 and the CESM1\_LENS ensemble mean (former minus latter), highlighting the internally driven impacts of TIO SSTAs.

896

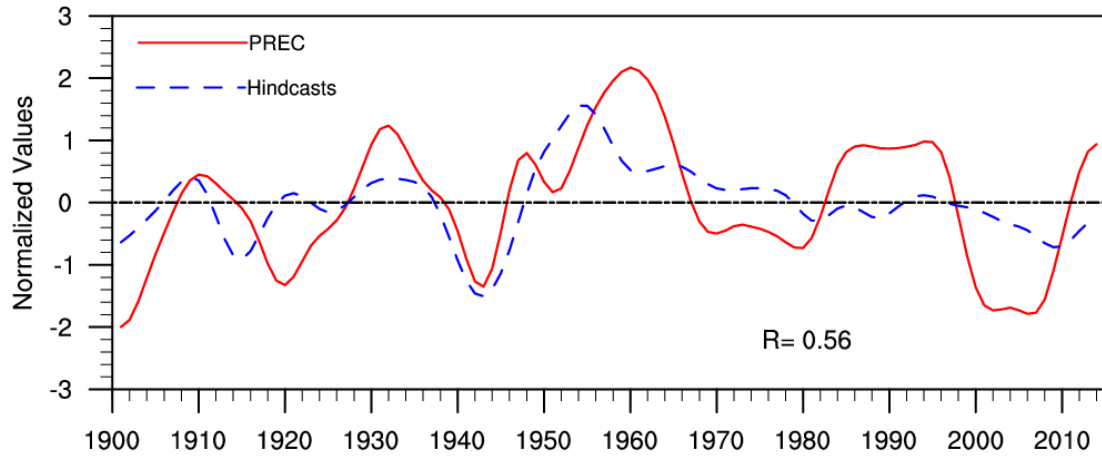
897

898

899

900

901



902

903

**Figure 11.** Normalized time series of the JJA-mean  $I_{EAMBZP}$  (red line) and associated leave-one-out cross-validated hindcast estimates (blue line) for 1901–2014, with the number denoting the TCC between the corresponding time series.

904

905

906

907

908

909

910

911

912

913

914

915

916

917

918

919

920

921

922

923

924

925

926

927

928

929

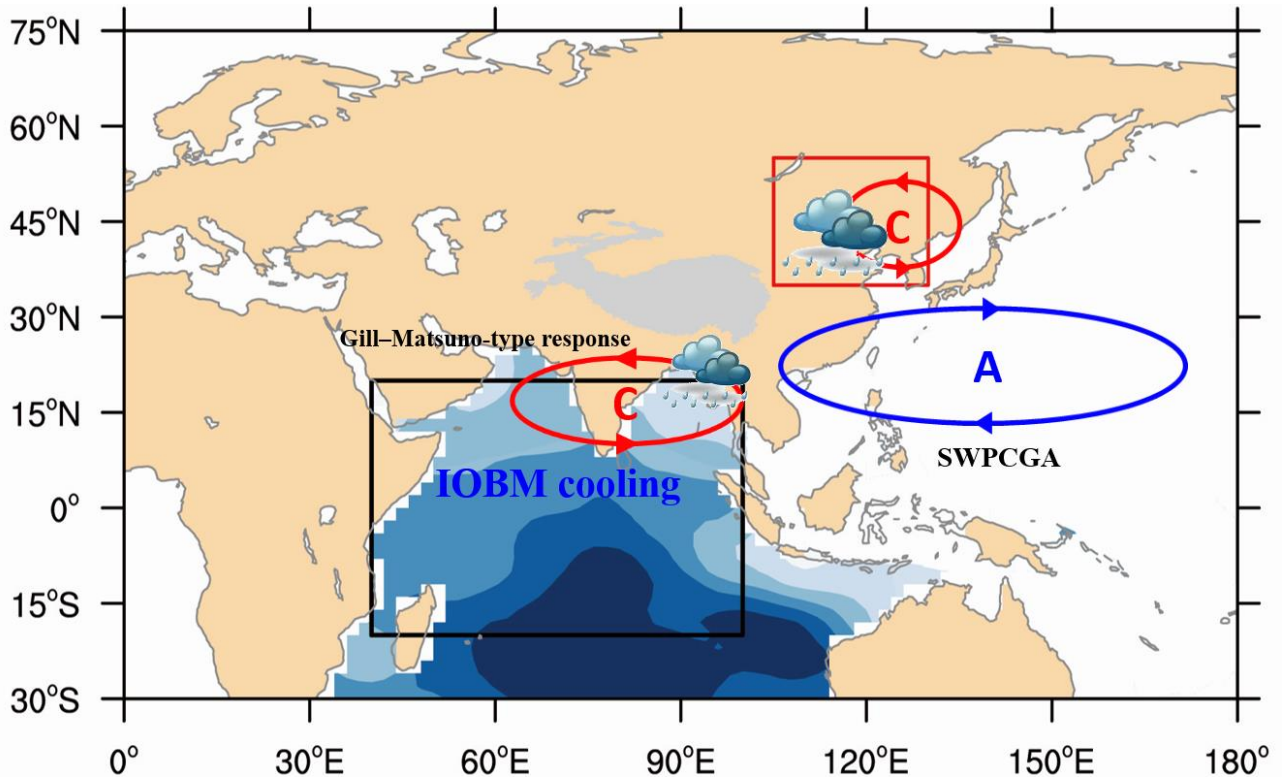
930

931

932

933

934



935

936

**Figure 12.** Schematic diagram showing how IOBM-related SST anomaly pattern drives the summer EAM precipitation fluctuations at interdecadal timescales. Blue shading illustrates the IOBM cooling. Letter A (C) indicates the center of the anticyclonic (cyclonic) gyre anomaly.

939

940

941

942